Editorial

Unraveling the Genomic Imprint of HBV in Hepatocarcinogenesis

*Hiroyasu Ito**

* Department of Joint Research Laboratory of Clinical Medicine, Fujita Health University, 1-98 Dengakugakubo, Kutsukake-cho, Toyoake, Aichi 470-1192, Japan.
E-mail: hiroyasu.ito@fujita-hu.ac.jp

〔Lab Med Int 2026; 5(1): 1-2〕

See article volume 5(1): 3-19

In this comprehensive review, Dr. Ogata presents a masterful synthesis of four decades of investigation into hepatitis B virus (HBV) integration and its role in hepatocellular carcinoma (HCC) development, a relationship first highlighted in early molecular studies. Advances in sequencing technologies—from Southern blotting and Sanger sequencing to second- and third-generation sequencing—have progressively refined our understanding of how HBV integrates into the human genome, particularly within repetitive genomic regions [1]. One of the most striking contributions detailed in this review is the discovery of HBV integration into centromeric alpha satellite DNA (αSat), first reported by Dr. Ogata. This finding was later reinforced by computational approaches such as SurVirus [2] and long-read sequencing analyses [3], which highlighted the centromere—previously inaccessible due to its repetitive structure—as a key locus where HBV-induced genomic instability may originate. The ability of HBV to integrate into αSat suggests a direct mechanism between viral infection, disruption of centromere function, and aneuploidy, widely observed in HCC. This review also places HBV integration within broader cancer genomics efforts including TCGA and ICGC projects, which revealed that HBV frequently targets major cancer-related genes such as *TERT*, *KMT2B*, and *CCNE1* [1,4]. Structural variations (SVs)—including chromosomal amplifications, deletions, and translocations—were shown to colocalize with HBV integration sites, with some SVs occurring decades before clinical HCC diagnosis [4]. Long-read sequencing has further clarified these events, revealing that HBV can induce not only local but also distant genomic alterations, reshaping the tumor genome in profound ways [3]. Beyond genomic mapping, emerging proteogenomic insights show that although HBV-derived proteins may be detectable in HCC tissues, their expression does not strongly correlate with clinical outcomes [5]. These results suggest that while HBV protein expression may diminish over time, the genomic scars left behind—such as HBV-driven SVs—continue to influence tumor biology. The clinical implications of these findings are likely to be significant. Advances in liquid biopsy technology—including methylated DNA assays and cfDNA-based repeat profiling—have enabled promising new avenues for early HCC detection [6]. Meanwhile, therapeutic strategies targeting telomerase, particularly anti-*TERT* approaches, have gained increasing traction due to the central role of *TERT* activation in HBV-related HCC [7]. Taken together, this review illustrates a cohesive narrative: HBV integration is not a random genomic event but a structured, biologically significant process that interacts with centromeric biology, genomic stability, and cancer evolution. As long-read sequencing and telomere-to-telomere genome assemblies mature, repetitive DNA elements—once viewed as "genetic dark matter"—are emerging as critical components in understanding HBV-mediated hepatocarcinogenesis [8]. This review not only synthesizes past knowledge but also illuminates future directions, urging deeper investigation into HBV integration within repetitive genomic elements and its implications for prevention, early detection, and personalized therapy of HBV-related HCC.

References

1) Totoki Y, Tatsuno K, Covington KR, et al. Trans-ancestry mutational landscape of hepatocellular carcinoma genomes.

Nat Genet. 2014; 46(12): 1267-73.
2) Rajaby R, Zhou Y, Meng Y, et al. SurVirus: a repeat-aware virus integration caller. Nucleic Acids Res. 2021; 49(6): e33.
3) Zhuo Z, Rong W, Li H, et al. Long-read sequencing reveals the structural complexity of genomic integration of HBV DNA in hepatocellular carcinoma. NPJ Genom Med. 2021; 6(1): 84.
4) Qian Z, Liang J, Huang R, et al. HBV integrations reshaping genomic structures promote hepatocellular carcinoma. Gut. 2024; 73(7): 1169-82.
5) Gao Q, Zhu H, Doung L, et al. Integrated proteogenomic characterization of HBV-related hepatocellular carcinoma. Cell. 2019; 179(2): 561-77.
6) Sun J, Sun X, He W, et al. A liquid biopsy approach detects HCC and identifies GJA4 as a potential biomarker for HBV-HCC via plasma cfDNA methylome profiling. Clin Epigenetics. 2025; 17(1): 98.
7) Ningarhari M, Caruso S, Hirsch TZ, et al. Telomere length is key to hepatocellular carcinoma diversity and telomerase addiction is an actionable therapeutic target. J Hepatol. 2021; 74(5): 1155-66.
8) Altemose N, Logsdon GA, Bzikadze AV, et al. Complete genomic and epigenetic maps of human centromeres. Science. 2022; 376(6588): eabl4178.

Review Article

Hepatitis B virus integration into chromosomes in hepatocellular carcinoma cells with a focus on centromeric alpha satellite DNA: Advances in molecular techniques reveal new insights into hepatocarcinogenesis

†Norio Ogata, MD, PhD[1, 2†]*

†Correspondence: *[1]Division of Laboratory Medicine, *[2] Division of Internal Medicine, Niigata Cancer Center Hospital, 2-15-3, Kawagishi-cho, Chuo-ward, Niigata city, Niigata 951-8566, Japan
Tel: +81-25-266-5111; Fax: +81-25-233-3849;
E-mail: nogata@niigata-cc.jp
Received August 15, 2025; accepted October 30, 2025
*[1] Division of Laboratory Medicine, *[2] Division of Internal Medicine, Niigata Cancer Center Hospital, 2-15-3, Kawagishi-cho, Chuo-ward, Niigata city, Niigata 951-8566, Japan

ABSTRACT

The molecular mechanisms by which hepatitis B virus (HBV) contributes to hepatocellular carcinoma (HCC) have been investigated since the late 1970s. This review follows advances in molecular biology and sequencing, particularly since the mid-2000s, which have enabled detailed analysis of HBV DNA integrations into the human genomes.

Molecular cloning and Sanger sequencing have identified that HBV integrates into several gene regions and non-genic regions, mainly repetitive sequences. Chromosomal rearrangements have also been observed. Our group first reported HBV integration into centromeric alpha satellite DNA (αSat) of HCC cells associated with genomic rearrangements. Second- generation (short-read) sequencing has found that many gene regions are involved in HBV integration with *TERT* promoter the most. Approximately 30 HCC-driver genes including *TERT*, *CTNNB1* and *TP53* have been identified. Third-generation (long-read) sequencing has revealed that driver genes are located not only close to HBV integration sites but also distant from HBV integration sites through structural variations (SVs). Also, 10-50% of HBV integrations have been confirmed to occur in centromeric or other repetitive regions, key loci for initiating SVs. Computational methods have emphasized that αSat may be the preferential locus for HBV integration. Recent completion of the full αSat sequence, the "real" goal of the Human Genome Project, allows better exploration of this underappreciated genome. Together, findings in this article refine current views of HBV-related hepatocarcinogenesis.

Ongoing advances in sequencing and centromeric biology are expected to deepen our understanding of virus-induced genomic instability and guide future strategies for early detection, prevention, and treatment of HBV-related HCC.

〔Lab Med Int 2026; 5(1): 3-19〕

Key Words

Hepatocellular carcinoma (HCC), Hepatitis B virus (HBV), α satellite DNA (α Sat), Centromere, Structural variation (SV)

I. Introduction

Epidemiological studies have clearly demonstrated a strong correlation between infection with hepatitis B virus (HBV) and the occurrence of hepatocellular carcinoma (HCC)[1)-3)].

Since the advent of molecular biological techniques applied to human genomes in the late 1970s, the causal relationship between HBV and HCC has been extensively studied. The discovery of HBV DNA integration into the chromosomes of human HCC tissues through Southern blot analysis suggested that integrated viral sequences might contribute to hepatocarcinogenesis.

Three key features have been proposed to define oncogenic viruses[4)]: (1) the presence and persistence of viral DNA or RNA in tumors, (2) the presence of viral oncogenes, and (3) the ability to modify host genes, through insertional mutagenesis (nearby genes) or chromosomal rearrangements (distant genes), which prompt activation of tumor-related genes or inactivation of tumor-suppressor genes.

This review summarizes breakthroughs in molecular biological techniques over the past few decades, that have advanced our understanding of HBV-related hepatocarcinogenesis. Particular emphasis is given to centromeric alpha satellite DNA (αSat) that we identified for the first time as a target of HBV DNA integration in HCC cells.

II. Southern blot analysis of HBV DNA in HCC

Beginning in the early 1980s, Southern blot analysis was widely used to examine the molecular state of HBV DNA in both HCC and non-malignant liver tissues[5)-8)].

Our representative results are shown in **Figure 1**. The HBV genome possesses a unique structure consisting of partially double-stranded DNA with a full genome length of 3.2 Kbp.

Typically, total DNA was extracted from HCC tissues and digested with restriction endonucleases, either those that do not cut within the HBV genome (e.g., *Hin*dIII or *Eco*RI) or those that do (e.g., *Bam*HI or *Bgl*II). The digested DNA was then subjected to agarose gel electrophoresis followed by Southern blot hybridization. Digestion with those restriction enzymes that do not cut HBV DNA allows the detection of integration forms of HBV DNA, which yield signals distinct from those of undigested DNA. Band signals indicate stable, fixed forms of HBV DNA present across clonal cell populations, while smeared signals suggest heterogenous structures of HBV DNA present among heterogenous cell populations. In some cases, replication forms of HBV DNA are also noticed in HCC tissues, which produce signals in both undigested- and enzyme-digested samples when the enzymes do not cut the viral genome, indicating active viral replication.

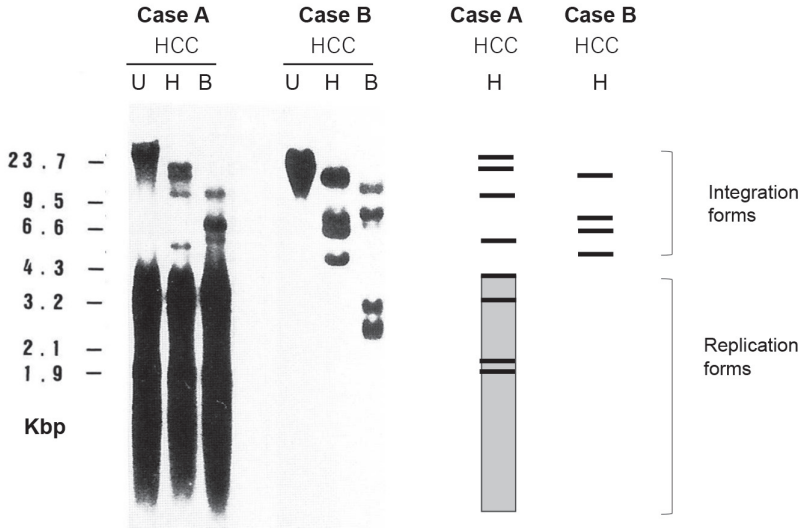

Figure 1 Representative findings of Southern blot hybridization of total DNA extracted from human HCC tissues for the presence and structures of HBV DNA. The extracted DNA (20 μg, each) was either undigested (U), digested with *Hin*dIII (H) or *Bam*HI (B), electrophoresed into 0.8% agarose gels and hybridized with a cloned HBV DNA probe. The *Hin*dIII is known to have no cutting site within the HBV genome, whereas BamHI possesses one cutting site within the HBV genome. Typical integration forms and replication forms of HBV DNA are illustrated at the right part of the figure.

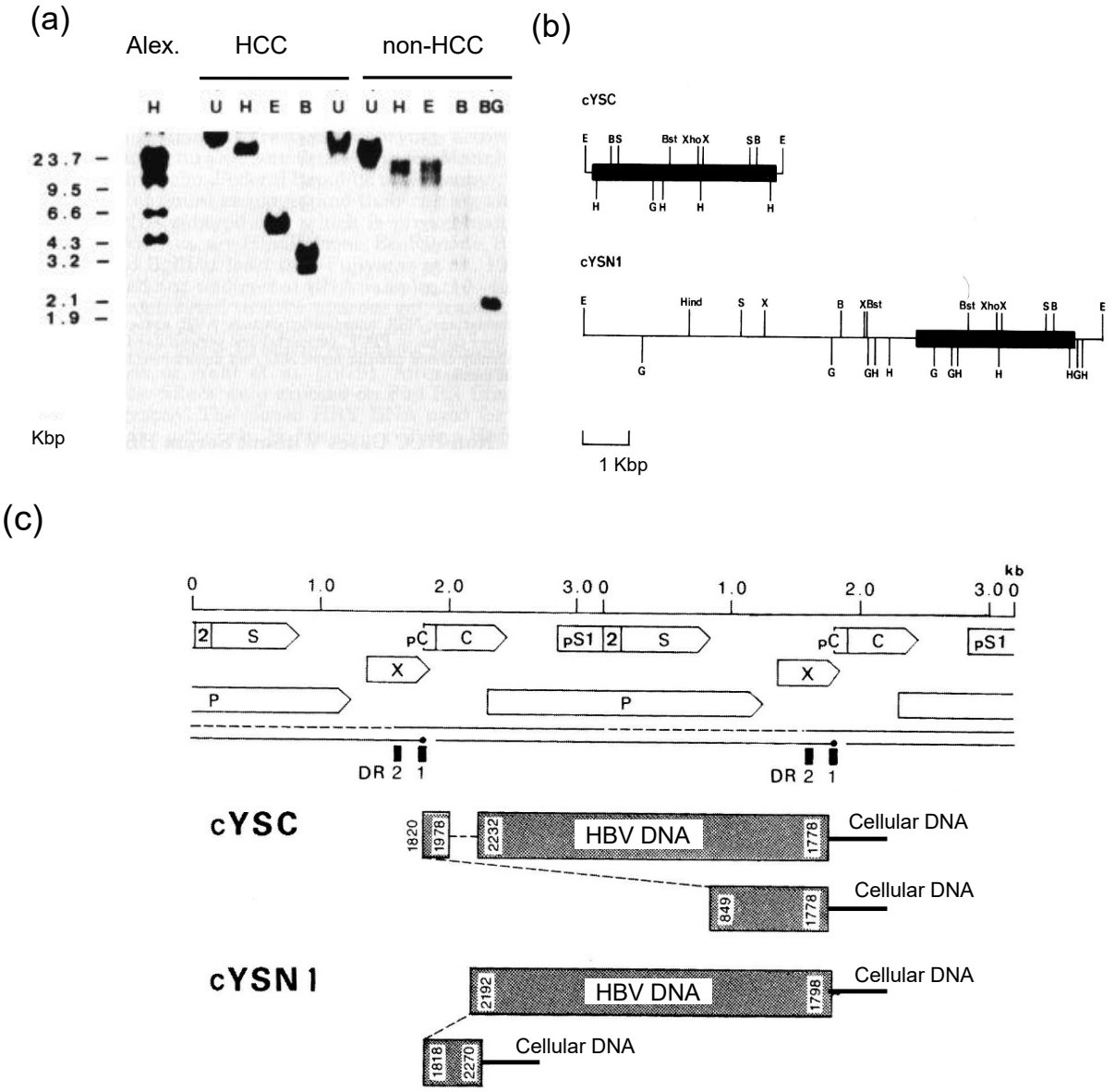

Figure 2

(a) Southern blot analysis of cellular DNA for the presence of HBV DNA. Alexander cell line (PLC/PRF/5 cells) was used as a positive control, of which lane is indicated as Alex. Total celluar DNA was extracted from Alexader cell lines. Also, total cellular DNA was extracted from HCC tissue and non-HCC tissue derived from the same patient. Extracted DNA (20 μg, each) was either undigested (U), digested with *Hin*dIII (H), *Eco*RI (E), *Bam*HI (B), or *Bgl*II (BG), electrophoresed into 0.8% agarose gels, blotted onto a nitrocellulose filter, and hybridized with a [α-^{32}P] cloned HBV DNA probe. *Hin*dIII and *Eco*RI have no cutting site within the HBV genome, *Bam*HI has one cutting site within the HBV genome, and *Bgl*II has more than two cutting sites within the HBV genome.

(b) Restriction endonuclease maps of cloned genomic DNA fragments derived from HCC tissue (cYSC) and from non-HCC tissue (cYSN1). Integrated HBV DNA is denoted by thick line; flanking cellular DNA by thin line. Cleavage sites with restriction endonucleases are indicated with the following abbreviations: E, *Eco*RI; B, *Bam*HI; Hind, *Hin*dIII; G, *Bgl*II; H, *Hinc*II; S, *Sph*I; Bst, *Bst*EII; Xho, *Xho*I, X, *Xba* I.

(c) Structure of the integrated HBV DNA sequences in the clones. In the upper part of the figure, tandem dimers of HBV genomes and coding regions with the direction of transcription of the structural genes are indicated with the following abbreviations; S = S gene coding for HBsAg; pS1 = preS1 region; 2 = preS2 region; C = C gene coding for HBcAg and HBeAg; pC = preC region; X = X gene; and P = P gene coding for a DNA polymerase / reverse transcriptase. The positions of the 11-bp direct repeats (DR2 and DR1) are indicated by small vertical bars that start at nucleotide positions 1590 and 1824, respectively. The region between DR2 and DR1 is the cohesive end region. In the lower part of the figure, organization of integrated HBV DNA clone from HCC tissue (cYSC) and non-HCC tissue (cYSN1) are illustrated by shaded bars with the nucleotide positions at each end. Deletion in the genome in cYSC is represented by a dashed line. The complex-type virus DNA that consists of two HBV genomes whose regions are overlapping, at least in part (cYSC and cYSN1), is represented by multiple solid bars aligned in different levels, each representing different units of the virus genome, and are connected by tilted dashed lines. In the clone cYSC, two incomplete HBV genomes are connected in an inverted manner at nucleotide positions 1820 and 849. Both virus-cellular junctions locate at the same nucleotide position 1778, between DR2 and DR1. In the clone cYSN1, two incomplete HBV genomes are also connected in an inverted manner at nucleotide positions 2192 and 1818. One virus-cellular junction locates at nucleotide position 1798, between DR2 and DR1, and another junction locates at nucleotide position 2270.

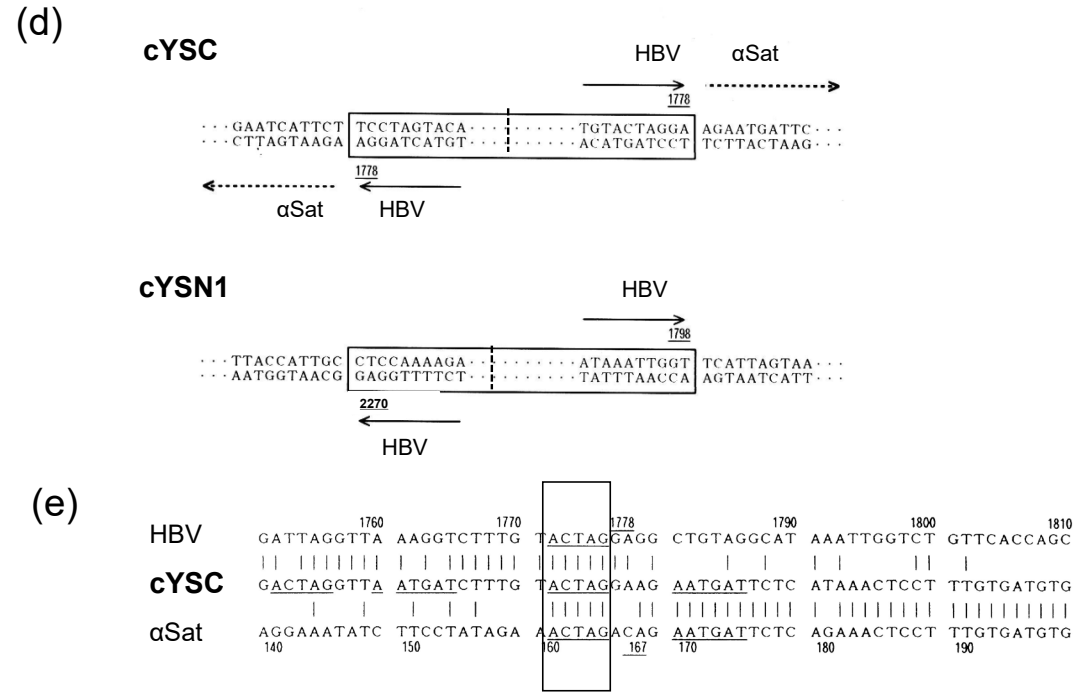

Figure 2 (continue)
(d) Nucleotide sequences around the junction region of HBV-host DNA in the integrated HBV DNA clone from the HCC tissue clone (cYSC) and non-HCC tissue clone (cYSN1). The HBV DNA sequences are boxed. The connection of the two incomplete HBV genomes is indicated by dashed line. In cYSC, HBV DNA and flanking host alpha satellite (αSat) sequences together formed an inverted structure. In cYSN1, the HBV DNA is inverted, but flanking cellular sequences are not inverted. Numbers underlined indicate nucleotide positions at the end of integrated HBV sequences. Arrowheads of solid lines indicate the direction of HBV transcription and those of dashed lines represent the 5' to 3' direction of monomeric units of αSat.
(e) Nucleotides sequences showing 5-bp microhomology (MH), ACTAG, between HBV DNA and αSat around the virus-cellular junction locus. The MH is presented by a box.

III. Sanger sequencing-based detection of HBV integration events

1. Case study: HBV integration into centromeric αSat in a young female patient with HCC

A 27-year-old Japanese woman, known to be a chronic HBV carrier with positive serum antibodies to HBe antigen (anti-HBe) and normal serum ALT values, developed HCC [7]. Total DNA was extracted from surgically resected HCC tissue and adjacent non-tumor tissue and subjected to Southern blot analysis. Histo-pathologically, the non-tumor tissue showed minimum or no necro-inflammatory reactions.

As shown in **Figure 2a**, following digestion with *Hin*dIII or *Eco*RI, enzymes that do not cut within the HBV genome, DNA from the HCC tissue showed a single band, indicating a clonal population harboring a uniform HBV DNA structure, whereas DNA from the non-tumor tissue exhibited a smeared pattern, suggesting heterogeneity in HBV DNA structure among non-cancerous hepatocytes. A DNA clone from HCC tissue (designated cYSC) and a DNA clone from non-tumor tissue (designated cYSN1) were molecularly cloned, subjected to generating restriction endonuclease mappings (**Figure 2b**) and sequenced using the Sanger method. Both clones showed similar integration structures, characterized by inverted HBV sequences, with host-viral DNA breakpoints located near the direct repeat 1 (DR1) and direct repeat 2 (DR2) regions, consistent with previous reports (**Figure 2c**). The flanking cellular DNA of cYSC was identical to αSat and surprisingly was also inverted along with the HBV genome (**Figure 2d**). Further analysis identified microhomology (MH) between HBV and αSat (**Figure 2e**), suggesting MH-mediated HBV integration.

A schematic diagram of the constituents of human centromere, including αSat, and changes of tandem repeats of αSat monomer caused by HBV integration in the presented case is shown in **Figure 3**.

Our findings are the first demonstrating centromeric αSat as a target for HBV DNA integration associated with inverted fusion of both viral and host repeat sequences [7].

2. Summary of direct cloning and Sanger sequencing studies

From the 1980s through the 1990s, a number of stud-

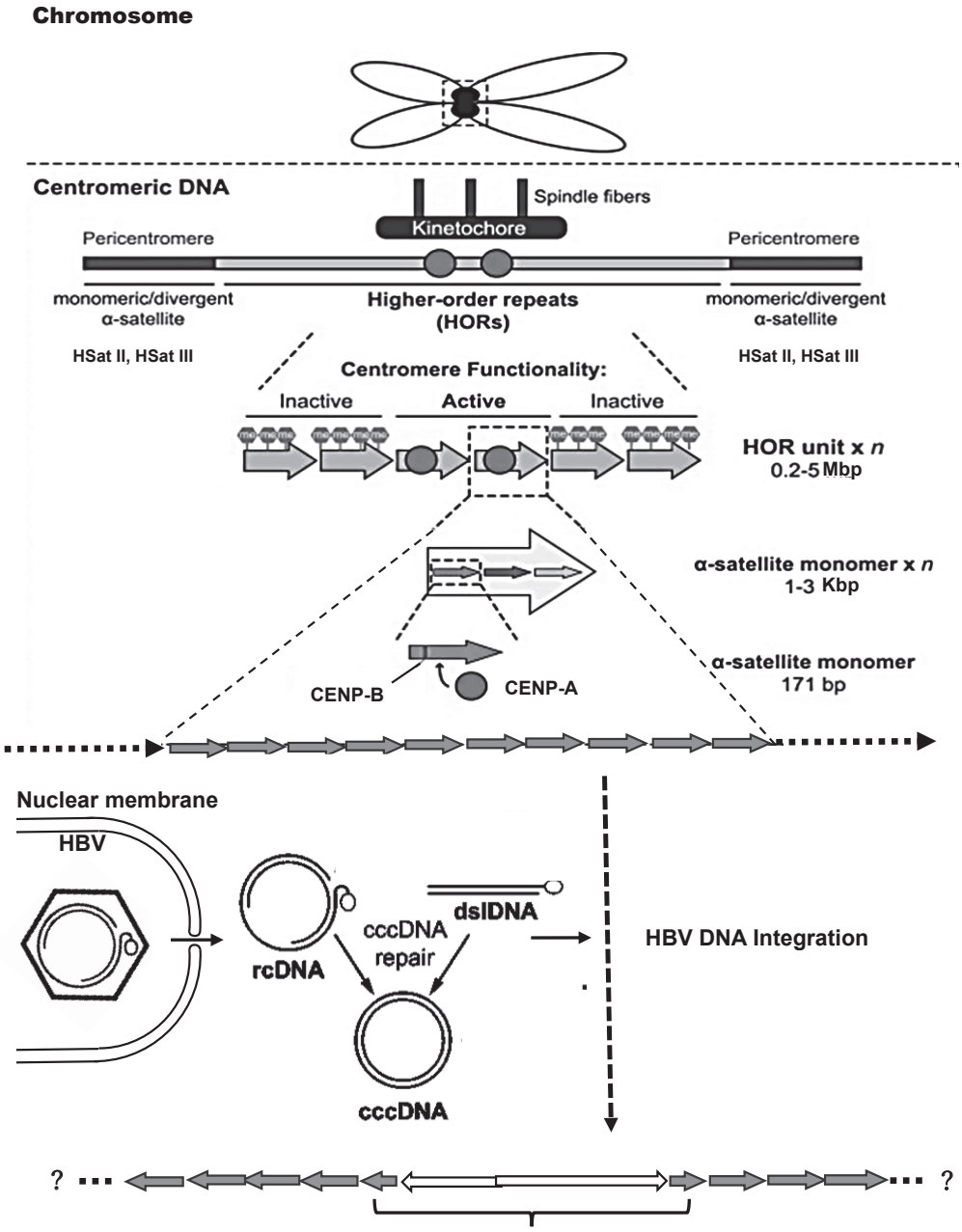

Figure 3 Human centromere structure and kinetochore organization. Human centromeres contain arrays of higher order repeats (HORs) of ~171-bp αSat monomers and arranged as a head-to-tail manner that can span several Mbp of DNA. Kinetochore proteins associate with only a subset of HOR units, which is called the active array. The functionally active centromere is defined epigenetically with centromeric protein (CENP)-A-containing nucleosomes. CENP-A plays central functions of the centromere in chromosome stability and segregation in mitosis. Some of αSat harbor a centromeric protein (CENP)-B binding motif (17-bp motif). CENP-B stabilizes the interaction between the chromatin and kinetochore. Pericentromeric regions contain monomeric or divergent αSat together with human satellite II (HSat II) / satellite III (HSat III) sequences and transposable elements.

Virions of HBV enter hepatocytes, then in the nucleus their genomes, either relaxed circular (rc) form or double-stranded linear (dsl) form, convert into covalently closed circular (ccc) form. All three HBV DNA molecules, rcDNA, dslDNA, and even cccDNA, can be molecular forms for integration into host chromosomes. In the HCC-derived clone in the patient presented in this article, after HBV DNA integration, structures of HBV DNA (possibly two genomes were integrated) underwent rearrangements together with franking αSat, resulting in an inverted fusion structure. Because the sequenced αSat region covered only a short part of the monomer, the extent of inverted repeat structure of αSat was not known.

Table 1 Summary of the results of altered chromosomal DNA regions in HCC cells, into which HBV integrated, that were analyzed using molecular cloning and Sanger sequencing.

gene region	clone No	Ref.	non-genic region	clone No	Ref.	chromosome	clone No	Ref.
erb-A/TR (*RARβ*)	1	10	minisatellite DNA	1	16	inversion	4	7, 25, 26
			satellite III DNA	4	17, 18	amplification	4	26, 27
erb-B (*EGFR*)	1	11	α satellite DNA	3	7, 19, 20	deletion / allelic loss	1	28
			long interspersed	2	13, 21	translocation		
cyclin A (*CCNA2*)	1	12	nuclear element			chr 17;18	1	29
			(LINE)			chr X;17	1	30
RBMY	1	13	short interspersed	8	18, 22, 23, 24	chr 5;9	1	30
p53 (*TP53*)	6	14, 15	nuclear element			chr 7p;17cen	1	19
			(SINE)			chr 3q;8p	1	31
						chr 17p;8p	1	32

No, number.
Current gene names are indicated in parenthesis.

ies used direct molecular cloning followed by Sanger sequencing to characterize integrated HBV DNA and its flanking host sequences. Much of this fundamental work was carried out by Prof. Kenichi Matsubara and colleagues at the Institute for Molecular and Cellular Biology, Osaka University [8) 9)].

A summary of these findings, including our owns, is provided in **Table 1**.

HBV integration sites were identified within or near the five gene regions, including four tumor-related genes involved in cell proliferation or cell cycle regulation and one tumor-suppressor gene, *TP53* [10-15)]. The infrequent detection of gene regions might be attributed to the fact that many genes had not yet been identified in those days.

HBV integration sites were found in non-genic regions more commonly, especially repetitive elements such as satellite DNAs, including αSat detected for the first time in our study, long interspersed nuclear elements (LINEs) of the *Kpn* family and short interspersed nuclear elements (SINEs) of the *Alu* family [7) 16-24)].

Chromosomal rearrangements were also observed in association with HBV integration [7) 19) 25-32)]. Among chromosome translocations, chromosome 17 carrying *TP53* tended to be frequently observed. Interestingly, in one case, the centromere of chromosome 17 served as the origin of a translocation to chromosome 7p [19)].

Thus, HBV integration can contribute both local and distant genomic alterations.

IV. Insights from second-generation (short-read) sequencing technologies (Illumina reads)

1. Impact of The Human Genome Project

In 1989, the White House of the United States announced the Human Genome Project (HGP), which began in 1990 and was completed in 2003. It successfully determined approximately 99% of the 2.85 Gbp nucleotide sequence in the human genome. The HGP used a clone-by-clone shotgun Sanger sequencing method. However, this method was unable to sequence centromeres, telomeres, and ribosome DNAs.

2. Advances of second-generation sequencing technology

Since the mid-2000s, next-generation sequencing, now called second-generation sequencing, has become available. This technology is approximately 300 times faster in analyzing sequences than the Sanger method. However, its limitations include short read lengths and difficulty in accurately aligning repetitive sequences.

In 2006, the National Institutes of Health in the USA launched The Cancer Genome Atlas (TCGA). This is the project to catalogue the genome alterations responsible for cancer. In 2008, for collaborating with world's leading researches of cancer and genomics the International Cancer Genome Consortium (ICGC) was established. Subsequent phases of ICGC included the Pan Cancer Analysis of Whole Genomes (PCAWG) in 2014 and Accelerating Research in Genomic Oncology (ARGO) in 2019.

Based on cited articles, in this review, HBV DNA integrations into gene regions are defined as those within exons, introns, or sequences within 10 Kbp away from the gene. HBV DNA integration is considered colocalized with host DNA structural variants (SVs), including copy number alterations (CNAs), if located within 500 Kbp. Driver genes are defined as genes with mutation frequencies that are statistically significant after accounting for background mutation rates.

Table 2 Summary of the results of altered chromosomal DNA regions in HCC cells, into which HBV integrated, that were analyzed using short-read (Illumina reads) sequencing .

Illumina reads						
	gene region	sample No	non-genic region	sample No	chromosome (gene)	Ref. 33
Patient No n=68	*TERT*	17	near the	ND	recurrent arm level gains in chr 1q, 5p, 6p, 8q	
	KMT2B	6	centromere		recurrent arm level losses in chr 1p, 4q, 6q, 8p, 17p	
	DQ582201	4	on chr 1p, 8p, 10q			
HBV-BP No n=628	*DDX11L11*	3			focal amplification: 25%:	
	DQ590432	2			30 genes (*TERT*, C*CND1*, *EGF19*, etc.)	
	ALOX5	2			homozygous deletion: 17%	
	MYO19	2			28 genes (*CDKN2A/2B*, *MAP2K3*, *PTEN*, etc.)	
	SENP5	2				
	RGS22	2			* relation to HBV integration : ND	
	ZFPM2	2				

Illumina reads						
	gene region	sample No	non-genic region	sample No	chromosome (gene)	Ref. 34
Patient No n=74	*TERT*	14	lnc RNA	ND	tandem duplication	
	KMT2B	5	*NEAT1*		deletion	
	SOX 5	2	*MALAT1/NEAT2*		translocation	
HBV-BP No n=233			CTCF-binding sites		38 genes (*TERT*, *CCND1*, *CDKN2A*, *ASH1L,* etc.)	
			* relation to HBV integratin: ND		* relation to HBV integration: ND	

High throughput viral integration detection (HIVID) method						
	gene region	sample No	non-genic region	sample No	chromosome (gene)	Ref. 38
Patient No n=426	*TERT*	101	preferentially	ND	HBV integration frequently at chr 5, 16, 17, 19	
	KMT2B	31	"repetitive"		especially at chr 17p (*TP53*, *MAP2K4/MMK4*)	
	FN1	17	or			
HBV-BP No n=3486	*CCNA2*	8	rare fragile sites			
	CCNE1	7				
	FAM 157A	7	satellite DNAs			
	PTPRD	2 ≤	tandem repetitive-			
	UNC5D	2 ≤	sequences			
	NRG3	2 ≤				
	CTNND2	2 ≤				
	AHDD	2 ≤				

No, number; BP, breakpoint; ND, not described.
Only recurrently altered gene regions are indicated.
Genes altered by chromosome rearrangements are indicated in parenthesis.

3. ICGC and HBV integration

As shown in **Table 2**, Totoki et al. [33] and Fujimoto et al. [34] contributed HCC sequencing data to the ICGC project. Totoki et al. [33] analyzed a multi-ethnic cohort (Japanese, Asian, and European), while Fujimoto et al. [34] focused exclusively on Japanese patients. Both studies included HCC cases of various etiologies, such as HBV, other viruses, and non-viral.

Regarding gene regions, Totoki et al. [33] identified 308 gene regions and Fujimoto et al. [34] found 94 gene regions, that were targeted by HBV integration, indicating the heterogeneity of HCC genomes. Both studies reported frequent HBV integrations in *TERT* and *KMT2B*. Totoki et al. [33] further analyzed *TERT* promoter mutations

and detected them in 54% (254 /469) of HCC cases, including 37% (44 /120) HBV-positive HCCs. The HBV integration and *TERT* promoter mutations were mutually exclusive. Collectively, *TERT* somatic alterations and enhanced expression were observed in ~70% of HCC cases.

Regarding non-genic regions, Totoki et al.[33] noted some HBV integrations near the centromeres on chromosomes 1p, 8p, and 10q, although frequency and detailed characterization were not reported. Fujimoto et al.[34] did not show HBV integration into repetitive sequences, but identified recurrent alterations in long non-coding RNAs (lncRNAs), such as *NEAT1* and *MALAT1* (*NEAT2*). However, their association with HBV integration was not described.

Chromosomal rearrangements (i.e., SVs including CNAs) occurred frequently in HCC. A broad range of tumor-related genes and tumor-suppressor genes were affected by these molecular events. Totoki et al.[33] reported several chromosomal arm-level gains and losses, affecting 30 genes with focal amplifications and 28 genes with homozygous deletions. Although these SVs were not mentioned in the context of HBV integration, the number of such SVs was found to be higher in HBV-related HCCs than in HCCs of broad range of other etiologies. Fujimoto et al.[34] reported several chromosomal rearrangements, such as tandem duplications, deletions, and translocations, affecting 38 genes with alterations. Although each SV was not described in relation to HBV integration, the number of HBV integration sites per sample was identified to be positively correlated with the number of SVs.

Based on significant alterations, 30 genes by Totoki et al.[33] and 25 genes by Fujimoto et al.[34], were selected as candidate driver-genes. Importantly, mutations in drug target kinase genes such as *EGFR1*, *EGFR2*, *FGFR3*, *KIT*, *JAK1,* and *MET* were rarely found in HCC[33, 34]. This observation suggests limited applicability of current cancer genomic medicine in patients with HCC.

To further explore the genomic landscape and its variability across populations, Shibata et al.[35] expanded upon these findings by incorporating two additional studies[36, 37]. They compiled genomic data of TCGA project from more than 1,000 publicly available HCC cases, which included 1,340 patients from different ethnic groups, including Japanese, Asian, and European cohorts.

In total, 33 driver genes were detected. The most frequently mutated gene region was *TERT* (~ 60%), followed by *CTNNB1* and *TP53* (each ~ 30%). Due to the high GC content of the *TERT* promoter regions, short-read Illumina sequencing had difficulty in detecting mutations, and thus the true frequencies of *TERT* region mutations could not be established. *TERT*, *CTNNB1,* and *TP53* were identified as master genes in HCC across all ethnic groups. The second most frequently (> 7%) mutated driver gene group included *ALB*, *APOB*, *ARID1A*, *ARID2,* and *AXIN1*. Remaining low frequency (< 5%) mutated driver gene group was involved in various biological functions.

Collectively, across the four referenced studies, SVs, including CNAs, occurred frequently in HCC cells and affected a broad range of tumor-related genes and tumor suppressor genes. Also, SVs significantly increased at HBV breakpoint locations, indicating that HBV integration contributed to gene alterations through chromosomal instability in HCC cells.

4. High-throughput viral integration detection

Zhao et al.[38] reported the sequencing results of patients with HBV-related HCC using the high throughput viral integration detection (HIVID) method from a Chinese cohort of 600 patients with HBV-related HCC. Briefly, HIVID uses HBV-specific probes to enrich viral DNA, followed by computational analysis based on TCGA dataset. (see Refs. 38, 39 for methodological details).

As shown in **Table 2**, the study by Zhao et al.[38] examined a relatively large number of patients with HBV-related HCC and studied HCC tissues and paired non-tumor tissues.

In gene regions, they identified 826 genes with HBV insertions in tumor samples and 303 in non-tumor samples, with only 64 genes shared between the two, highlighting distinct integration profiles in tumor versus non-tumor tissues. Notably, there were as many as 88 genes recurrently affected in HCC, many of which were previously unreported. Examples included *PTPRD*, *UNC5D*, *NRG3*, *CTNND2*, and *AHRR*. Expression changes were noticed both at the transcript and protein levels, suggesting that these novel affected genes were functionally relevant to HBV insertion.

Interestingly and importantly, HCCs arising from non-cirrhotic liver displayed a significantly enriched HBV integration in the vicinity of *KMT2B*, *CCNE1*, and *AHDD*.

In non-genic regions, HBV integration occurred preferentially in satellite DNAs and tandem repetitive sequences, possibly including LINEs and SINEs. This is the first study to report that HBV preferentially integrates into repetitive or fragile genomic regions, including satellite DNAs.

Regarding chromosomal rearrangements, HBV integration was significantly enriched in chromosomes 5,16,17,

and 19, especially chromosome 17p, which harbors *TP53* and a newly identified *MAP2K4* (*MKK4*).

Clinically, circulating HBe antigen (HBeAg) levels were positively correlated with the number of HBV integrations in HCC tissues, suggesting that higher HBV replication activity increases the likelihood of integration.

V. Computational tools for detecting HBV integration in repetitive regions: Insertion or integration callers

As described previously, short-read sequencing technologies face inherent limitations, particularly in mapping reads to repetitive genomic regions. When multiple similar copies of a region exist throughout the genome, aligners often fail to determine the correct location, as multiple potential alignment sites can exist for a single read. This challenge becomes especially critical when a virus integrates into repetitive sequences, leading to misaligned or ambiguously mapped reads.

Several computational programs have been developed to analyze large-scale sequencing datasets for viral integration events, but they struggled to accurately predict integrations in repeat-rich regions of the host genome. Among available computational methods, SurVirus has been identified as a particularly sensitive, precise, and efficient virus integration caller to achieve precise results. Using a second-generation paired-end sequencing dataset, along with a host genome reference and a viral database, SurVirus predicts integration events that occurred, providing the precise integration loci on the host genome and the corresponding viral segments involved (see Refs. 40, 42, and 43 for methodological details).

Rajaby et al.[40] applied SurVirus to analyze HBV using the HBV HIVID database[38] and the HBV whole-genome sequencing (WGS) dataset[41]. Among approximately 500 detected HBV insertion events, 7% were novel, and most occurred in repeat regions. Among these HBV insertions, satellite DNAs accounted for 40% of the insertions, followed by LINEs (15%) and SINEs (0.5%).

Because Rajaby and colleagues[40),42),43)] extensively published on similar computational algorisms for detecting insertion elements in host genomes[42),43)], their findings are considered robust and reliable. Importantly, this study is the first to highlight the significant role of repetitive sequences in hepatocarcinogenesis, indicating the need for computational tools capable of resolving complex genome regions.

VI. Findings from third-generation (long-read) sequencing technologies (PacBio or Nanopore reads)

1. Overview of third-generation sequencing

While second generation sequencing technology enabled analyses of HBV integration in HCC, their reliance on short reads introduces several limitations. These include the inability to directly sequence full-length viral genomes, sensitivity to probe-capture bias, sequencing depth, and analysis methods. Importantly, short-read technologies struggle with tandem repeats and repetitive sequences, often leading to errors in sequencing, alignment, assembly, or amplification. This makes it challenging to determine the exact sequence composition and number of repeat units within each repetitive region.

In the mid-2010s, third generation sequencing methods, including PacBio and Nanopore reads, have become available, providing long reads (~20 Kbp). These long-reads enabled more accurate mapping of integration events, especially in complex genomic regions.

2. Key studies using short- and long- read sequencing

As shown in **Table 3**, recent studies, ranging both short-read (Illumina reads) and long-read (PacBio or Nanopore reads) sequencing, have provided crucial insights into HBV integration patterns.

Ethnicities of patients with HBV-related HCC in each report were as follows; Zhuo et al.[44] studied a Chinese cohort, Alverti et al.[45] analyzed a Japanese cohort, Peneau et al.[46] examined multi-ethnic (European, African, and Asian) cohort, and Qian et al.[47] studied a Chinese cohort.

Regarding gene regions, altered gene regions were essentially similar to previous reports, and further, confirmed that HBV enhancers induced high mRNA expression. Important findings from these studies can be summarized as follows; First, HBV integration in the promoter region of *TERT* was not detected in non-tumor tissues[44]. Second, tumors harboring HBV integrations in *CCNE1*, *CCNA2*, or *KMT2B* were more frequently identified in patients without cirrhosis[46]. Third, *KMT2B*-integrated HCCs did not show alterations in the *TERT* promoter or other known driver genes[46], suggesting that *KMT2B*-altered HCC may involve distinct mechanisms of carcinogenesis. Fourth, among young patients with HCC (< 35 years old), *TERT* mutations (1.9%) and *CCNE1* mutations (3.7%) were rare, while over half of these patients had alterations in *TP53*[47]. Thus, in HCCs from a subgroup of patients without cirrhosis, alterations of one or two genes may induce strong proliferation, replication stress, and a rearrangement signature that

Table 3 Summary of the results of altered chromosomal DNA regions in HCC cells, into which HBV integrated, that were analyzed using short-read (Illumina reads) and long-read (PacBio or Nanopore reads) sequencing.

Illumina reads						**Nanopore or PacBio reads**		Ref.
	gene region	sample No	non-genic region	sample No	chromosome		chromosome (gene)	44
Patient No ND	*CCNE1*	153	"repeat sequences"	265	ND	Patient No ND	"complex" all autosomal chromosomes except for chr 15, 16, 21 priority on chr 1, 4, 5, 19	
	TERT	17						
	SYT14	27						
HBV-BP No n=475	*SERTADO*	7				HBV-BP No n=141		
	LINCO 1493	2						
	MIR 12125	2						
	MIR 4457	2						

Illumina reads						**Nanopore reads**		Ref.
	gene region	sample No	non-genic region	sample No	chromosome (gene)		chromosome (gene)	45
Patient No n=51	*TERT*	14	ND	ND	chr 5p amplification (*TERT*)	Patient No n=7/9	translocation chr 1p;9p with chr 1p deletion (*ARID1A*) chr 1p;11q chr 3p;Xq with chr Xp deletion (*RPS6KA3*) chr 4q;7q with (one patient: chr 4q deletion (*IRF2*); chr 8q;4p; chr 8q;10q) chr 8q;13q wirh chr 13q deletion (*RB1*) chr 8p;17p with chr 17p deletion (*TP53*) chr 11q;19p	
	KMT2B	4						
	CCNE1	2						
HBV-BP No n=148								

Illumina reads						**PacBio reads**		Ref.
	gene region	sample No	non-genic region	sample No	chromosome (gene)		chromosome (gene)	46
Patient No n=177	*TERT*	48	centromere/ peri-centromere	10-20 %	chr 17p deletion (*TP53*) :15 cases 8/15 centromere**	Patient No n=3	inverted duplication : 1 sample translocation : 2 samples isochromosome ** : 1 sample	
	CCNE1	4						
	KMT2B	3						
HBV-BP No n=2199	*AHRR*	2			chr 5p amplification (*TERT*) :14 cases	HBV-BP No n=8	amplification: chr 5p (*TERT*), 8q (*MYC*) deletion: chr 17p (*TP53*)	
	NRG1	2						
	TRIM16L	2			chr 8q amplification (*MYC*) :13 cases 4/13 centromere**			
	ST18	2						

Illumina reads						**Nanopore reads**		Ref.
	gene region	sample No	non-genic region	sample No	chromosome (gene)		chromosome (gene)	47
Patient No n=84	*TERT*	28	teromere or centormeric satellite DNA	15%	chr 17p deletion near centromere** (*TP53*)	Patient No n=50	large duplication : 10 samples inverted fusion: 54 samles translocation : 59 samples	
	KMB2	7						
	CCNE1	2						
HBV-BP No n=482	*TSHZ2*	2			chr 8q amplification and / or chr 8p deletion	HBV-BP No n=298	amplification: chr 5p (*TERT*), 8q (*MYC*), 19q, 1q, 7p, 6p, 20q deletion: chr 17p (*TP53*), 8p, 4q, 16q, 6q, 9p (*CDKN2A*), 13q (*RB*), 1p (*ARID1A*)	

No, number; BP, breakpoint; ND, not described; ** HBV integration into centromere
Only recurrently altered gene regions are indicated.
Genes altered by chromosome rearrangements are indicated in parenthesis.

directly promotes cancer development. Further, in HCCs in a subgroup of younger patients, different mechanisms other than common gene alterations may develop cancer. Collectively, these findings suggest that distinct mechanisms may underlie HBV-related HCC development across ethnic groups, non-cirrhotic liver states and age cohorts.

Regarding non-genic regions, Zhuo et al.[44] reported that more than half, 55.8% (265 /475) of HBV breakpoints in tumors were located within repetitive sequences. The frequency of such breakpoints was higher in tumor tissues than in non-tumor tissues. Although the specific characteristics of these repetitive sequences were not clearly identified, these findings suggest that preferential HBV integration into chromosomal repetitive sequences may confer a selective advantage during tumorigenesis. Additionally, Peneau et al.[46] found that approximately 10-20% of HBV breakpoints were located in centromeric or pericentromeric regions. Also, Qian et al.[47] reported that approximately 15% of HBV breakpoints were in telomere or centromeric satellite DNAs. These results indicate that HBV integration into centromeric regions is more frequent than previously reported.

Several studies have reported a relationship between viral insertion events and SVs. For example, Peneau et al.[46] reported that 36% of HBV integration events precisely matched SV boundaries. Three major types of SVs that were bordered by HBV integration in more than 40 samples included deletion of chromosome 17p and amplification of chromosomes 5p and 8q. Notably some of these SVs involved centromeric regions. Qian et al.[47] reported that deletion of chromosome 17p occurred near an HBV-integrated centromere.

In these reports, despite the use of short-read sequencing, a relatively high percentage of HBV integrations into repetitive sequences was observed compared to previous studies. While the reason for this discrepancy remains unclear, possibly improved sequencing performance may partly explain the difference.

Using long-read sequencing, detailed insights into the contributions of HBV integration to SVs have been obtained. Peneau et al.[46] reported that HBV integration-related SVs were prevalent in 41% of HCCs and 48% of them were associated with CNAs. Qian et al.[47] reported that HBV integration-related CNAs occured in 58% of HCCs, especially enriched in younger patients. Both studies identified common CNAs at the chromosome arm level as well as focal copy number changes affecting key cancer-related genes.

In case reports, Alverti et al.[45] reported detailed results. They studied nine Japanese patients with HCC, in whom only one end of the integrated HBV DNA was detected using short-read sequencing. Among these, seven patients showed non-canonical integration involving chromosomal translocations.

Peneau et al.[46] examined three patients with non-canonical integration. They found several types of SVs, including an intriguing finding of generating isochromosome of 8q, which might be caused by HBV integration into centromere.

Qian et al.[47] studied many patients with non-canonical integration. They identified several types of SVs, including amplifications and deletions in a large number of chromosomes, which were accompanied by HBV integration.

Peneau et al.[46] and Qian et al.[47] investigated HBV-integration events in relation to clinical aspects.

Peneau et al.[46] identified a larger amount of replicating HBV DNA in non-tumor tissues correlated with a higher number of HBV integration in HCC cells. They further found the number of HBV integration generating CNAs-was an independent prognostic factor in HCC progression.

Qian et al.[47] compared CNAs between HBsAg-positive and HBsAg-negative groups. HBsAg-positive tumors showed significantly more frequent ($p<0.02$) amplification of chromosome 8q and deletions in chromosomes 4q, 16q, and 17p, which were among the most common HBV-associated CNAs. Although not all chromosomes were studied, these results suggest a contribution of HBV integration-associated CNAs to HCC development. They also reconstructed the likely evolutionary scenario timelines of HBV-integration-induced amplification in chromosome 8q, using changes in the number of the clock-like mutations using COSMIC SBS signature 1 and 5 before and after the amplification. Their results suggested that most of these amplifications likely occurred decades prior to the clinical diagnoses, some as early as before age 10. They proposed that HBV-integration-induced CNAs, especially by ultra-early chromosome 8q amplifications, may promote the initial clonal expansion, shorten the time to malignant transformation, or accelerate tumor progression through the combined effects of viral proteins and overexpression of oncogenic hotspot genes. They also observed a significant correlation between higher HBV DNA levels and *TP53* mutation. Based on these findings, they emphasized importance of early antiviral therapy to prevent HBV-driven genomic alterations.

Collectively, long-read sequencing has revealed that not only gene-regions close to HBV integration sites but also those located at considerable distances from HBV inte-

gration sites can be altered through HBV-related SVs. Importantly, centromeric regions appear to contribute to the generation of multiple SVs, as previously reported by our group [7] and others [19] during the early era of molecular biology using direct cloning and Sanger sequencing.

While many HBV integrations may represent passenger events, some act as cancer drivers that promote HCC initiation. Long-read sequencing is emerging as an essential tool in HBV integration pattern research and may have future research and possibly clinical applications. It is particularly valuable for elucidating HBV integration patterns including SVs and clonal expansion, and finally, the underlying mechanisms of HBV-induced carcinogenesis.

VII. Characterization of genomics and proteomics of integrated HBV

1. Structural features of integrated HBV

It is widely believed that most integrated HBV sequences are derived from the normal double-stranded linear (dsl) DNA and primarily through MH-mediated mechanisms [48]. Li et al. [49] by analyzing long-read sequencing data from 35 HBV-related patients with HCC, identified several structural patterns of HBV integration. In their study, both ends of the integrated HBV fragments were captured using long-read sequencing. Notably, short HBV insertion segments (0–1 Kbp) accounted for ~50% of integration events, while longer viral segments (>3 Kbp) accounted for ~25% of such events. The longest detected HBV insertion measured 5,408 bp.

Normally generated HBV dslDNA is speculated to be in the range of 1816–3182/1–1832. The dslDNA is thought to be difficult to cross the 1600–1900 bp region. However, Li et al. [49] found the HBV insertion fragment in the range from 843 to 2263 of HBV genome. Notably, some integration events included complete pre-surface (S) 1/pre S 2/S gene or pre-core (C)/C gene.

Therefore, they speculated several mechanisms of virus integration as follows. (1) The reverse transcription process leads to the formation of excessively redundant HBV dslDNA sequences, which are integrated into the human genome through the classical non-homologous end joining or MH-mediated end joining (MMEJ) mechanism. (2) The abnormally redundant HBV single-stranded DNA is integrated into the human genome through the single-strand annealing mechanism. (3) The closed circular HBV genome is integrated into the human genome through the MMEJ mechanism.

Due to limited research on the characteristics and mechanisms of HBV integration, the integration mechanism of HBV sequence remains unclear.

2. Mutations and genotypes of integrated HBV

Peneau et al. [46] unexpectedly observed a negative selection of HBV variants that impair HBeAg production, including mutations in the basic core promoter locus and pre-core region [50) 51] or mutations associated with antiviral resistance in reverse transcriptase domains [52] in HBV sequences integrated into HCC genomes. This observation suggests that while these mutations may enhance viral fitness or facilitate immune escape, they do not provide a specific advantage for tumor development.

Qian et al. [46] investigated the genotypes of integrated HBV in a diverse population where nearly all major HBV genotypes (A, B, C, D, E, F, G, and H) were present. Among the integrated HBV sequences, genotype C was the most prevalent, followed by genotype B.

3. Transcripts and proteins of integrated HBV

As part of the Clinical Proteomic Tumor Analysis Consortium, a comprehensive proteogenomic analysis of HBV-related HCCs in a Chinese cohort was performed by Gao et al. [53].

Gao et al. [53] reported that the large envelope protein, external core antigen/capsid protein, and polymerase were detected in both proteomic and RNA sequencing datasets, while the X protein was not detected, but only mRNA was detected. These results raise questions about the role of the X protein in HCC, suggesting that it may not be essential for the maintenance of the malignant phenotype. There were less abundant HBV mRNAs and proteins in HCC tissues than in non-HCC liver tissues. The presence of HBV proteins in HCC tissues did not correlate with the survival of patients with HCC.

They also detected significantly lower protein and mRNA levels of the HBV receptor NTCP (sodium taurocholate co-transporting polypeptide) in HCC tissues than in non-HCC liver tissues. Unlike HBV proteins, reduced NTCP expression in HCC tissue was significantly associated with reduced survival, indicating its potential relevance in disease progression.

VIII. αSat and centromeric biology

1. Complete sequencing of αSat

Human centromeres are located within large arrays of tandemly repeated DNA sequences known as α Sat, which often span millions of base pairs (Mbp) on each chromosome. Although HGP was declared completion in 2003, several genomic regions remained unresolved due to sequencing limitations. These included centromeric, telomeric, and ribosomal DNA regions. The "real" completion of HGP was achieved in 2022 under the telomere-to-telomere assembly project [54), 55]. In this assembly, satellite

repeats constitute 6.2% of the human genome assembly, with αSat representing the largest component, 2.8% of the genome [54]. Each αSat array is more likely to interact with centromere protein A (CENP-A), an essential inner kinetochore protein required for normal chromosome segregation during mitosis [56]. With the availability of complete αSat sequences, the structure and function of αSat DNA have become a rapidly growing area of research, particularly in the context of human diseases, including cancers.

2. Centromere function and its role in aneuploidy

Aneuploidy, defined as an abnormal number of chromosomes, is a hallmark of cancer, that was first described well over a century ago [57]. The causes of aneuploidy have been understood as chromosome instability, resulting in the gain or loss of chromosomes or chromosome fragments. The centromere breakage is a major initiating factor leading to aneuploidy and the resulting changes in the selective landscape that drive most cancers [57].

In this context, HBV DNA integration into αSat sequences, particularly when accompanied by the reforming may disrupt the structural integrity of αSat. This disruption could directly contribute to the generation of aneuploidy by impairing normal centromere function and chromosome segregation.

IX. Clinical Implications

1. Translation of genetic landscapes into clinical practice

Comprehensive molecular and genomic analyses of large HCC cohorts have now uncovered the landscape of driver genes, characteristic mutational signatures, and molecular classification of tumor subtypes. To translate this growing body of knowledge for better diagnosis, treatment, and prevention of this intractable cancer subtype, further advances are needed in genetic screening and clinical sequencing to facilitate early diagnostic tools, such as liquid biopsy, to optimize and individualize treatment strategies, and to accelerate translational drug developments, especially targeting *TERT* (anti-*TERT* drugs), which may represent a promising avenue.

2. Liquid biopsy

Liquid biopsy detects cell free (cf) and/or circulating tumor (ct) DNA, which reflects various types of biological information from the tumor and serves as sensitive tools for non-invasive detection of early-stage HCC [58].

Methylated cf/ctDNA is a cancer-specific DNA fragment that is one of the most advanced tools for early HCC detection.

Suehiro et al. [59] have developed a new assay called combine restriction digital PCR (CORD) assay, which enables counting each copy of a methylated gene in a small amount of DNA. Using this assay, Kotoh et al. [60] found that the median copy number of methylated *SEPT9* (m-*SEPT9*) was significantly higher in patients with HCC than patients with chronic liver diseases and healthy volunteers. This assay showed a sensitivity of 63% and a specificity of 90% for detecting HCC across all stages. A meta-analysis performed by Chandrapalan et al. [61] included six case-control studies of m-*SEPT9* conducted in Japan as mentioned above as well as in the USA and in Europe and showed a pooled sensitivity of 80% and a pooled specificity of 90% for detecting HCC of all stages. Thus, m-*SEPT9* has shown promise in detecting HCC with high estimated diagnostic performance.

Chalasani et al. [62), 63)] have researched methylated marker sets of three genes, *HOXA1*, *B3GALT6*, and *TSPYL5*, combined with sex and serum level of α fetoprotein (AFP) (designated mt-HBT). This algorithm showed a sensitivity of 82% and a specificity of 87% for detecting early-stage HCC. Kunimune at al. [64] have examined a methylated marker of a gene, *HOXA1*, combined with age, sex, and serum levels of AFP together with des-γ-carboxyl prothrombin (DCP) (designated ASDAmH-1). This index demonstrated a sensitivity of 76% and a specificity of 78% (non-viral HCC) and 75% (viral HCC) for detecting early-stage HCC. Performances of the two methods were not affected by HCC ethiology and demonstrated similar numerical values.

Mutations of the *TERT* promoter and other driver gene regions have been studied for liquid biopsy. Qu et al. [65] have studied an assay using WGS followed by target-gene amplification using primers covering *TERT* promoter, *TP53*, *CTNNB1*, *AXIN1*, and HBV integration breakpoint in plasma cfDNA. They constructed an assay combining these gene mutations with serum levels of AFP and DCP (designated HCCscan). This assay showed a good sensitivity and a specificity for detecting HCC. Although the low positive predictive value for the occurrence of HCC (17%) warrants improvement, this assay poses a trigger point for visualizing mutations in driver gene regions in cfDNA.

Variations of α Sat and other repetitive sequence have been investigated for liquid biopsy. Annapragada et al. [66] have developed a method called an alignment-free, genome-wide approach for analyzing repeat elements in diseases (ARTEMIS), which uses short k-mer sequences in plasma cfDNA. This method successfully identified tumor-specific changes in repeat elements, including centromeric satellite DNAs, LINEs, SINEs, long terminal repeats, and

transposable elements in cfDNA in early-stage HCC and lung cancer among more than ten kinds of cancers investigated. This method is a good example of emerging αSat and other repetitive sequences in the clinical fields of cancers in cfDNA.

Alterations of chromosomes have been examined for liquid biopsy. Zhang et al. [67] have improved an approach called DNA evaluation of fragments for early interception (DELFI), which constructs WGS and analyzes the degree of DNA fragmentation in plasma cfDNA. This approach was revealed to be useful for distinguishing chromosome lengths in cfDNA in early-stage HCC. This assay is a representative breakthrough toward identifying chromosomal gains and losses in cancers in cfDNA.

MicroRNAs (miRNAs) are essentially 18 to 22-nucleotide-long endogenous noncoding RNAs. The effects of miRNAs on the regulation of expression of various genes are very broad. Several reports have shown aberrant expression of specific miRNAs. Circulating blood miRNAs, which are highly stable in a cell-free form, have shown promise as novel potential biomarkers for the early detection of HCC and there have been several miRNAs that have been demonstrated to be useful in the HCC diagnosis [68), 69)].

Among several miRNAs, miR-122 is a liver-specific, highly expressed miRNA [70)]. A meta-analysis performed by Zhao et al. [71)] has shown that miR-122 confered moderate efficacy for discriminating patients with HCC from healthy controls or patients with HBV infection. Furthermore, Trung et al. [72)] reported that combination assays of circulating miR-122 and *TERT* promoter exhibited satisfactory diagnostic performance in discriminating patients with HCC from other patients.

3. Therapy using anti-*TERT*

Therapies that target telomerase have been viewed as a highly attractive means of cancer treatment. The disruption of the telomerase maintenance mechanism is important in achieving replicative immortality, which is fundamental characteristics in various cancers, including HCC. Recent main telomerase-targeting therapies are antisense oligonucleotides (ASO), nucleoside analogues (NA), small molecule inhibitors, and stabilizers of G-quadruplexs (see Refs 73, 74 for revews)

Among these, ASO and NA have recently been reported as promising candidates for HCC therapy.

Ningarhari et al.[75)] found that ASO was efficient in highly proliferative and poorly differentiated cells. This revealed oncogenic addiction to *TERT* in HCC, providing a rationale for anti-*TERT* ASO treatment in HCC.

Mender et al. [76), 77)] reported that NA, 6-thio-dG (THIO), which was concerted into the corresponding 5'-triphosphate and incorporated into telomeres by telomerase, was effective in controlling tumor growth, especially when combined with immune check-point inhibitors in a T cell-dependent manner, providing a rationale for combining anti-*TERT* NA therapy and immunotherapy in HCC.

X. Perspectives

Robust HBV replication activity measured by peripheral serum HBeAg and HBV DNA levels has been significantly correlated with increased frequency of HBV integration events. Because such a virological state can persist for decades (e.g., the immune-tolerant phase of chronic HBV infection following neonatal infection), individuals with persistent HBV infection may experience a long window period during which hepatocarcinogenesis is initiated.

It is likely that the initiation of HBV-related HCC, one of the cancers driven by viral genome-integration, differs fundamentally from cancers of non-viral genome-integration etiology, including other forms of HCC. HBV may act as a molecular trigger that directly interacts with critical host genomic elements in hepatocytes [6), 8)]. Depending on the context, these interactions may induce genomic or proteomic alterations that activate carcinogenic signaling pathways, ultimately driving tumorigenesis in ways that are similar to other cancer types.

Fortunately, current preventive strategies such as vaccination [78), 79)] and antiviral therapy [80)] can prevent HCC occurrence. Antiviral therapy in the early life of HBV-infected individuals, together with further development in molecular and biological technologies supported by the complete human genome sequence, including αSat, is expected to eliminate HBV-related HCC.

Conflicts of interest

The author declares no conflict of interest.

Funding

None

References

1) Maupas P, Melnick JL. Hepatitis B infection and primary liver cancer. Prog Med Virol. 1981; 27: 1-5.

2) Beasly RP. Hwang LY, Lin CC, et al. Hepatocellular carcinoma and hepatitis B virus. A prospective study of 22 707 men in Taiwan. Lancet. 1981; 2 (8256): 1129-33. doi: 10.1016/s0140-6736 (81) 90585-7.

3) Chen C-J, Yang H-I, Su J, et al. Risk of hepatocellular carcinoma across a biological gradient of serum hepatitis B virus DNA level. JAMA. 2006; 295 (1): 65-73. doi: 10.1001/jama 295.1.65.

4) Zapatka M, Borozan I, Brewer DS, et al. The landscape of viral associations in human cancers. Nat Genet. 2020; 52 (3) : 320-30. doi: 10.1038/s41588-019-0558-9. Epub 2020 Feb 5.
5) Ogata N, Ichida F, Hamada C, et al. Mode of integration of hepatitis B virus DNA in chronically infected lives with indications of multiclonal growth of hepatocytes and some hepatoma cells. In: Zuckermann AJ, editor. Viral Hepatitis and Liver Disease. New York: Ala R. Liss, Inc; 1988. p. 746-51.
6) Ogata N. Mechanisms of hepatocarcinogenesis induced by hepatitis viruses: HBV DNA integration into hepatocytes and development of hepatocellular carcinoma. In: Ichida F, editor. New Development of Research of Liver Disease. Vol. III3 Tokyo: Medical View; 1998. p. 211-26. (In Japanese)
7) Ogata N, Tokino T, Kamimura T, et al. A comparison of the molecular structure of integrated hepatitis B virus genomes in hepatocellular carcinoma cells and hepatocytes derived from the same patient. Hepatology. 1990; 11 (6) : 1017-23. doi: 10.1002/hep.1840110617.
8) Matsubara K, Tokino T. Integration of hepatitis B virus DNA and its implications for hepatocarcinogenesis. Mol Biol Med. 1990; 7 (3) : 243-60.
9) Fujiyama A, Miyanohara A, Nozaki C, et al. Cloning and structural analyses of hepatitis B virus DNAs, subtype adr. Nucleic Acids Res. 1983; 11 (13) : 4601-10. doi: 10.1093/nar/11.13.4601.
10) Dejean A, Bougueleret L, Grzeschik KH, et al. Hepatitis B virus DNA integration in a sequence homologous to v-erb-A and steroid receptor genes in a hepatocellular carcinoma. Nature. 1986; 322 (6074) : 70-2. doi: 10.1038/322070a0.
11) Zhang XK, Egan JO, Huang D, et al. Hepatitis B virus DNA integration and expression of an erb B-like gene in human hepatocellular carcinoma. Biochem Biophys Res Commun. 1992; 188 (1) : 344-51. doi: 10.1016/0006-291x (92) 92391-a.
12) Wang J, Chenivesse X, Henglein B, et al. Hepatitis B virus integration in a cyclin A gene in a hepatocellular carcinoma. Nature. 1990; 343 (6258) : 555-7. doi: 10.1038/343555a0.
13) Tsuei D-J, Chang M-H, Chen P-J, et al. Characterization of integration patterns and flanking cellular sequences of hepatitis B virus in childhood hepatocellular carcinomas. J Med Virol. 2002; 68 (4) : 513-21. doi: 10.1002/jmv.10240.
14) Zhou YZ, Slagle BL, Donehower LA, et al. Structural analysis of a hepatitis B virus genome integrated into chromosome 17p of a human hepatocellular carcinoma. J Virol. 1988; 62 (11) : 4224-31. doi: 10.1128/JVI.62.11.4224-4231.1988
15) Slagle BL, Zhou YZ, Butel JS. Hepatitis B virus integration event in human chromosome 17p near the p53 gene identifies the region of the chromosome commonly deleted in virus-positive hepatocellular carcinomas. Cancer Res. 1991; 51 (1) ; 49-54.
16) Berger I, Shaul Y. Integration of hepatitis B virus: analysis of unoccupied sites. J Virol. 1987; 61 (4) : 1180-6. doi: 10.1128/JVI.61.4.1180-1186.1987.
17) Shaul Y, Garcia PD, Schonberg S, et al. Integration of hepatitis B virus DNA in chromosome-specific satellite sequences. J Virol. 1986; 59 (3) : 731-4. doi: 10.1128/JVI.59.3.731-734.1986.
18) Nagaya T, Nakamura T, Tokino T, et al. The mode of hepatitis B virus DNA integration in chromosomes of human hepatocellular carcinoma. Genes Dev. 1987; 1 (8) : 773-82. doi: 10.1101/gad.1.8.773.
19) Meyer M, Wiedorn KH, Hofschnerider PH, et al. A chcomosome 17:7 translocation is associated with a hepatitis B virus DNA integration in human hepatocellular carcinoma DNA. Hepatology. 1992; 15 (4) : 665-71. doi: 10.1002/hep.1840150419.
20) Tsuei DJ, Hsu TY, Chen JY, et al. Analysis of integrated hepatitis B virus DNA and flanking cellular sequences in a childhood hepatocellular carcinoma. J Med Virol. 1994; 42 (3) : 287-93. doi: 10.1002/jmv.1890420316.
21) Quade K, Saldanha J, Thomas H, et al. Integration of hepatitis B virus DNA through a mutational hot spot within the cohesive region in a case of hepatocellular carcinoma. J Gen Virol. 1992; 73 (Pt 1) : 179-82. doi: 10.1099/0022-1317-73-1-179.
22) Fowler MJ, Thomas HC, Monjardino J. Cloning and analysis of integrated hepatitis B virus DNA of the adr subtype derived from a human primary liver cell carcinoma. J Gen Virol. 1986; 67 (Pt 4) : 771-5. doi: 10.1099/0022-1317-67-4-771.
23) Matsumoto H, Yoneyama T, Mitamura K, et al. Analysis of integrated hepatitis B virus DNA and cellular flanking sequences cloned from a hepatocellular carcinoma. Int J Cancer. 1988; 42 (1) : 1-6. doi: 10.1002/ijc.2910420102.
24) Chen JY, Harrison TJ, Tsuei DJ, et al. Analysis of integrated hepatitis B virus DNA and flanking cellular sequences in the hepatocellular carcinoma cell line HCC36. Intervirology. 1994; 37 (1) : 41-6. doi: 10.1159/000150355.
25) Mizusawa H, Taira M, Yaginuma K, et al. Inversely repeating integrated hepatitis B virus DNA and cellular flanking sequences in the human hepatoma-derived cell line huSP. Proc Natl Acad Sci USA. 1985; 82 (1) : 208-12. doi: 10.1073/pnas.82.1.208.
26) Yagimuma K, Kobayashi M, Yoshida E, et al. Hepatitis B virus integration in hepatocellular carcinoma DNA: duplication of cellular flanking sequences at the integration site. Proc Natl Acad Sci USA. 1985; 82 (13) : 4458-62. doi: 10.1073/pnas.82.13.4458.
27) Pineau P, Marchio A, Mattei MG, et al. Extensive analysis of duplicated-inverted hepatitis B virus integration in human hepatocellular carcinoma. J Gen Virol. 1998; 79 (Pt 3) : 591-600. doi: 10.1099/0022-1317-79-3-591.
28) Rogler CE, Sherman M, Su CY, et al. Deletion in chromosome 11p associated with a hepatitis B integration site in hepatocellular carcinoma. Science. 1985; 230 (4723) : 319-22. doi: 10.1126/science.2996131.
29) Hino O, Shows TB, Rogler CE. Hepatitis B virus integration site in hepatocellular carcinoma at chromosome 17;18 translocation. Proc Natl Acad Sci USA. 1986: 83 (21) ; 8338-42. doi: 10.1073/pnas.83.21.8338.

30) Tokino T, Fukushige S, Nakamura T, et al. Chromosomal translocation and inverted duplication associated with integrated hepatitis B virus in hepatocellular carcinomas. J Virol. 1987; 61(12): 3843-54. doi: 10.1128/JVI.61.12.3843-3854.1987.

31) Pineau P, Marchio A, Terris B, et al. A t(3;8) chromosomal translocation associated with hepatitis B virus integration involves the carboxypeptidase N locus. J Virol. 1996; 70(10): 7280-4. doi: 10.1128/JVI.70.10.7280-7284.1996.

32) Becker SA, Zhou YZ, Slagle BL. Frequent loss of chromosome 8p in hepatitis B virus-positive hepatocellular carcinomas form China. Cancer Res. 1996; 56(21): 5092-7.

33) Totoki Y, Tatsuno K, Covington KR, et al. Trans-ancestry mutational landscape of hepatocellular carcinoma genomes. Nat Genet. 2014; 46(12); 1267-73. doi: 10.1038/ng.3126. Epub 2014 Nov 2.

34) Fujimoto A, Furuta M, Totoki Y, et al. Whole-genome mutational landscape and characterization of noncoding and structural mutations in liver cancer. Nat Genet. 2016; 48(5): 500-9. doi: 10.1038/ng.3547. Epub 2016 Apr 11.

35) Shibata T, Arai Y, Totoki Y. Molecular genomic landscapes of hepatobiliary cancer. Cancer Sci. 2018; 109(5): 1282-91. doi: 10.1111/cas.13582. Epub 2018 Apr 28.

36) Schulze K, Imbeaud S, Letouzé E, et al. Exome sequencing of hepatocellular carcinomas identifies new mutational signatures and potential therapeutic targets. Nat Genet. 2015; 47(5): 505-11. doi: 10.1038/ng.3252. Epub 2015 Mar 30.

37) Cancer Genome Atlas Research Network. Comprehensive and integrative genomic characterization of hepatocellular carcinoma. Cell. 2017; 169(7): 1327-41. e23. doi: 10.1016/j.cell.2017.05.046.

38) Zhao L-H, Liu X, Yan H-X, et al. Genomic and oncogene preference of HBV integration in hepatocellular carcinoma. Nat Commun. 2016; 7: 12992. doi: 10.1038/ncomms12992.

39) Li W, Zeng X, Lee NP, et al. HIVID: an efficient method to detect HBV integration using low coverage sequencing. Genomics. 2013; 102(4): 338-44. doi: 10.1016/j.ygeno.2013.07.002. Epub 2013 Jul 15.

40) Rajaby R, Zhou Y, Meng Y, et al. SurVirus: a repeat-aware virus integration caller. Nucleic Acids Res. 2021; 49(6): e33. doi: 10.1093/nar/gkaa1237.

41) Sung W-K, Zheng H, Li S, et al. Genome-wide survey of recurrent HBV integration in hepatocellular carcinoma. Nat Genet. 2012; 44(7): 765-9. doi: 10.1038/ng.2295.

42) Rajaby R, Liu D-X, Au CH, et al. INSurVeyor: improving insertion calling from short read sequence data. Nat Commun. 2023; 14(1): 3243. doi: 10.1038/s41467-023-38870-2.

43) Rajaby R, Sung W-K. SurVIndel2: improving copy number variant calling from next-generation sequencing using hidden split reads. Nat Commun. 2024; 15(1): 10473. doi: 10.1038/s41467-024-53087-7.

44) Zhuo Z, Rong W, Li H, et al. Long-read sequencing reveals the structural complexity of genomic integration of HBV DNA in hepatocellular carcinoma. NPJ Genom Med. 2021; 6(1): 84. doi: 10.1038/s41525-021-00245-1.

45) Álvarez EG, Demeulemeester J, Otero P, et al. Aberrant integration of hepatitis B virus DNA promotes major restructuring of human hepatocellular carcinoma genome architecture. Nat Commun. 2021; 12(1): 6910. doi: 10.1038/s41467-021-26805-8.

46) Péneau C, Imbeaud S, Bella TL, et al. Hepatitis B virus integrations promote local and distant oncogenic driver alterations in hepatocellular carcinoma. Gut. 2022; 71(3): 616-26. doi: 10.1136/gutjnl-2020-323153. Epub 2021 Feb 9.

47) Qian Z, Liang J, Huang R, et al. HBV integrations reshaping genomic structures promote hepatocellular carcinoma. Gut. 2024; 73(7): 1169-82. doi: 10.1136/gutjnl-2023-330414.

48) Bill CA, Summers J. Genomic DNA double-strand breaks are targets of hepadnaviral DNA integration. Proc Natl Acad Sci USA. 2004; 101(30): 11135-40. doi: 10.1073/pnas.0403925101.

49) Li W, Wei W, Hou F, et al. The integration model of hepatitis B virus genome in hepatocellular carcinoma cells based on high-throughput long-read sequencing. Genomics. 2022; 114(1): 23-30. doi: 10.1016/j.ygeno.2021.11.025. Epub 2021 Nov 26.

50) Ogata N, Miller RH, Ishak KG, et al. The complete nucleotide sequence of a pre-core mutant of hepatitis B virus implicated in fulminant hepatitis and its biological characterization in chimpanzees. Virology. 1993; 194(1): 263-76. doi: 10.1006/viro.1993.1257.

51) Ogata N, Miller RH, Ishak KG, et al. Genomic and biological characterization of two hepatitis B virus variants: A pre-core mutant implicated in fulminant hepatitis and a surface mutant resistant to immunoprophylaxis. In: Nishioka K, Suzuki H, Mishiro S, et al., editors. Viral Hepatitis and Liver Disease. Tokyo: Springer-Verlag; 1994. p. 238-42.

52) Ogata N, Fujii K, Takigawa S, et al. Novel patterns of amino acid mutations in the hepatitis B virus polymerase in association with resistance to lamivudine therapy in Japanese patients with chronic hepatitis B. J Med Virol. 1999; 59(3): 270-6.

53) Gao Q, Zhu H, Dong L, et al. Integrated proteogenomic characterization of HBV-related hepatocellular carcinoma. Cell. 2019; 179(2): 561-77. e22. doi: 10.1016/j.cell.2019.08.052.

54) Altemose N, Logsdon GA, Bzikadze AV, et al. Complete genomic and epigenetic maps of human centromeres. Science. 2022; 376(6588): eabl4178. doi 10.1126/science.abl4178. Epub 2022 Apr 1.

55) Altemose N. A classical revival: Human satellite DNAs enter the genomics era. Semin Cell Dev Biol. 2022; 128: 2-14. doi: 10.1016/j.semcdb.2022.04.012. Epub 2022 Apr 27.

56) Nassar R, Thompson L, Fouquerel E. Molecular mechanisms protecting centromeres from self-sabotage and implications for cancer therapy. NAR Cancer. 2023; 5(2): zcad019. doi: 10.1093/narcan/zcad019. eCollection 2023 Jun.

57) Zheng Y, Ahmad K, Heinkoff S. Total whole-arm chromosome losses predict malignancy in human cancer. Proc Natl

Acad Sci USA. 2025; 122(18): e2505385122. doi: 10.1073/pnas.2505385122. Epub 2025 May 2.

58) Lee Y-T, Fujiwara N, Yang JD, et al. Risk stratification and early detection biomarkers for precision HCC screening. Hepatology. 2023; 78(1): 319-62. doi: 10.1002/hep.32779. Epub 2022 Oct 11.

59) Suehiro Y, Hashimoto S, Higaki S, et al. Blood free-circulating DNA testing by highly sensitive methylation assay to diagnose colorectal neoplasias. Oncotarget. 2018; 9(24): 16974-87. doi: 10.18632/oncotarget.24768.

60) Kotoh Y, Suehiro Y, Saeki I, et al. Novel liquid biopsy test based on a sensitive methylated *SEPT9* assay for diagnosing hepatocellular carcinoma. Hepatol Commun. 2020; 4(3): 461-70. doi: 10.1002/hep4.1469. eCollection 2020 Mar.

61) Chandrapalan S, Bannaga A, Weidner A, et al. A systematic review and meta-analysis: the diagnostic accuracy of methylated *SEPTIN9* for the detection of hepatocellular carcinoma and the clinical evaluation of its use in combination with other surveillance modalities. Scand J Gastroenterol. 2022; 57(4): 473-80. doi: 10.1080/00365521.2021.2020331. Epub 2021 Dec 25.

62) Chalasani NP, Ramasubramanian TS, Bhattacharya A, et al. A novel blood-based panel of methylated DNA and protein markers for detection of early-stage hepatocellular carcinoma. Clin Gastroenterol Hepatol. 2021; 19(12): 2597-605.e4. doi: 10.1016/j.cgh.2020.08.065. Epub 2020 Sep 2.

63) Chalasani NP, Porter K, Bhattacharya A, et al. Validation of a novel multitarget blood test shows high sensitivity to detect early stage hepatocellular carcinoma. Clin Gastroenterol Hepatol. 2022; 20(1): 173-82.e7. doi: 10.1016/j.cgh.2021.08.010. Epub 2021 Aug 13.

64) Kunimune Y, Suehiro Y, Saeki I, et al. Combination assay of methylated *HOXA1* with tumor markers shows high sensitivity for detection of early-stage hepatocellular carcinoma. Liver Cancer. 2024; 13(5): 487-97. doi: 10.1159/000536211. eCollection 2024 Oct.

65) Qu C, Wang Y, Wang P, et al. Detection of early-stage hepatocellular carcinoma in asymptomatic HBsAg-seropositive individuals by liquid biopsy. Proc Natl Acad Sci USA. 2019; 116(13): 6308-12. doi: 10.1073/pnas.1819799116. Epub 2019 Mar 11.

66) Annapragada AV, Niknafs N, White J, et al. Genome-wide repeat landscapes in cancer and cell-free DNA. Sci Transl Med. 2024; 16(738): eadj9283. doi: 10.1126/scitranslmed.adj9283. Epub 2024 Mar 13.

67) Zhang X, Wang Z, Tang W, et al. Ultrasensitive and affordable assay for early detection of primary liver cancer using plasma cell-free DNA fragmentomics. Hepatology. 2022; 76(2): 317-29. doi: 10.1002/hep.32308. Epub 2022 Jan 26.

68) Yamamoto Y, Kondo S, Matsuzaki J, et al. Highly sensitive circulating microRNA panel for accurate detection of hepatocellular carcinoma in patients with liver disease. Heptol Commun. 2019; 4(2): 284-97. doi: 10.1002/hep4.1451. eCollection 2020 Feb.

69) Jin Y, Wong YS, Goh BKP, et al. Circulating microRNAs as potential diagnostic and prognostic biomarkers in hepatocellular carcinoma. Sci Rep. 2019; 9(1): 10464. doi: 10.1038/s41598-019-46872-8.

70) Masaki T, Arend KC, Li Y, et al. miR-122 stimulate hepatitis C virus RNA synthesis by altering the balance of viral RNAs engaged in replication versus translation. Cell Host Microbe. 2015; 17(2): 217-28. doi: 10.1016/j.chom.2014.12.014. Epub 2015 Feb 5.

71) Zhao X-F, Li N, Lin D-D, et al. Circulating microRNA-122 for the diagnosis of hepatocellular carcinoma: A meta-analysis. Biomed Res Int. 2020: 5353695. doi: 10.1155/2020/5353695. eCollection 2020.

72) Trung NT, Hoan NX, Trung PQ, et al. Clinical significance of combined circulating TERT promoter mutations and miR-122 expression for screening HBV-related hepatocellular carcinoma. Sci Rep. 2020; 10(1): 8181. doi: 10.1038/s41598-020-65213-8.

73) Suzuki H, Mishra S, Paul S, et al. Molecular and immune landscape of hepatocellular carcinoma for therapeutic development. J Liver Cancer. 2025; 25(1): 9-18. doi: 10.17998/jlc.2024.12.02. Epub 2024 Dec 6.

74) Gao J, Pickett HA. Targeting telomerases: Advances in telomere maintenance mechanism-specific cancer therapies. Nat Rev Cancer. 2022; 22(9): 515-32. doi: 10.1038/s41568-022-00490-1. Epub 2022 Jul 5.

75) Ningarhari M, Caruso S, Hirsh TZ, et al. Telomere length is key to hepatocellular carcinoma diversity and telomerase addiction is an actionable therapeutic target. J Hepatol. 2021; 74(5): 1155-66. doi: 10.1016/j.jhep.2020.11.052. Epub 2020 Dec 15.

76) Mender I, Siteni S, Barron S, et al. Activating an adaptive immune response with a telomerase-mediated telomere targeting therapeutic in hepatocellular carcinoma. Mol Cancer Ther. 2023; 22(6): 737-50. doi: 10.1158/1535-7163.MCT-23-0039.

77) Mender I, Girotti R, Gryaznov S. Nobel telomere-targeting dual-pharmacophore dinucleotide prodrugs for anticancer therapy. Nucleic Acids Res. 2025; 53(12): gkaf591. doi: 10.1093/nar/gkaf591.

78) Wong G L-H, Hui V W-K, Yip T C-F, et al. Universal HBV vaccination dramatically reduces the prevalence of HBV infection and incidence of hepatocellular carcinoma. Aliment Pharmacol Ther. 2022; 56(5): 869-77. doi: 10.1111/apt.17120. Epub 2022 Jul 21.

79) Ogata N, Cote PJ, Zanetti AR, et al. Licensed recombinant hepatitis B vaccines protect chimpanzees against infection with the prototype surface gene mutant of hepatitis B virus. Hepatology. 1999; 30(3): 779-86. doi: 10.1002/hep.510300309.

80) Udompap P, Kim WR. Development of hepatocellular carcinoma in patients with suppressed viral replication: changes in risk over time. Clin Liver Dis (Hoboken). 2020; 15(2): 85-90. doi: 10.1002/cld.904. eCollection 2020 Feb.

Original

Differentiation of mulberry bodies (cells) from oval fat bodies using distinct fat staining methods

Tsukasa Nozaki[*1], *Taku Kusaka*[*1], *Kentaro Wakamatsu*[*2,3], †*Satomi Asai*[*2]

†Department of Laboratory Medicine, Tokai University School of Medicine, 143 Shimokasuya, Isehara City, Kanagawa 259-1193, Japan
Tel: +81 463 93 1121 Ex. 2450; Fax: +81 463 93 8607;
E-mail: sa@tokai.ac.jp
Received July 22, 2025; accepted October 20, 2025
*1 Clinical Laboratory of Tokai University Hospital, 143 Shimokasuya, Isehara City, 259-1193, Japan
*2 Department of Laboratory Medicine, Tokai University School of Medicine, 143 Shimokasuya, Isehara City, 259-1193, Japan
*3 Department of Respiratory Medicine, National Hospital Organization, Omuta National Hospital, Fukuoka, Japan

ABSTRACT

Objective: The detection of mulberry bodies (cells) in urine facilitates the early diagnosis of Fabry disease. However, their detection is difficult because of their very small size and various shapes when stained with Sternheimer's staining. We investigated methods to specifically detect the various appearances of mulberry bodies (cells).

Methods: The urinary sediments of patients with Fabry disease were subjected to Sternheimer's staining, and the mulberry bodies (cells) and oval fat bodies were compared using four fat staining methods (Sudan III, Oil Red O, Nile blue, and Sudan black B).

Results: Differentiation between mulberry bodies (cells) and oval fat bodies using Sternheimer's, Sudan III staining was difficult. In contrast, they were clearly identified and distinguished when Nile blue and Sudan black B staining was performed. From the perspective of differentiating from OFBs, Sudan III and Oil Red O seemed more useful, as they show clear differences in stainability. On the other hand, for positively staining mulberry cells themselves, Nile blue and Sudan black B appear useful.

Conclusions: Mulberry bodies (cells) have various appearances. Although they are difficult to distinguish from oval fat bodies, they can be identified using Sudan III and Oil Red O, Nile blue and Sudan black B staining.

〔Lab Med Int 2026; 5(1): 20-24〕

Key Words
mulberry body, Fabry disease, urinary sediment, fat staining

INTRODUCTION

Fabry disease is a rare lysosomal storage disorder caused by a deficiency of the lysosomal enzyme alpha-galactosidase A (α-galactosidase A; α-GAL), resulting in the accumulation of glycolipids such as globotriaosylceramide (GL-3) in various cells [1)2)]. Accumulation of glycolipids in the urine of these patients results in the formation of circular, berry-like structures called mulberry bodies (cells). The detection of mulberry bodies in urine has been used as an indicator for early diagnosis of this disease [3)4)]. When stained with the Sternheimer method, mulberry bodies (cells) in urinary sediments exhibit a whorl-like appearance, making it an inexpensive and sensitive method used in routine laboratory practice [5)]. However, it is difficult to detect mulberry bodies (cells) and differentiate them from oval fat bodies (OFBs) using this method because they are very small and have various appearances.

In the present study, we evaluated staining methods to improve detection and differentiation of mulberry bodies (cells).

MATERIALS AND METHODS

Clinical Specimens

Urine specimens from three patients with Fabry disease, admitted to Tokai University Hospital, were analyzed in this study. The diagnosis of Fabry disease was confirmed by demonstration of deficiency in α-GAL activity. Oval fat bodies were obtained from urine samples of patients with nephrotic syndrome, specifically those with diabetic nephropathy

This study was approved by the Institutional Review Board for Clinical Research of Tokai University Hospital (14R-022) and conformed to the principles outlined in the Declaration of Helsinki.

Appearance of Mulberry Bodies (Cells) After Sternheimer Staining

The Sternheimer staining method was applied to urinary sediments and examined at 400 × magnification, as routinely used in our laboratory. The microscopic findings of mulberry bodies (cells) and urinary sediments were compared.

Comparison of Four Fat Staining Methods

Four fat staining methods were used to compare the stainability: Sudan III, Oil Red O, Nile blue, and Sudan black B (Muto Pure Chemicals Co., Ltd. Tokyo, Japan). Sudan black B staining was performed by mixing the stock solution with preservation buffer at a ratio of 3:2, and the solution was filtered prior to use. For staining, 10 mL of the patient's urine was centrifuged for 5 min at 500 × g, the supernatant was removed using an aspirator, and several drops of the stain solution were added to the sediment. The staining times for each staining method were as follows: Sudan III at 37 ℃ for 60 minutes; Oil Red O at 37℃ for 15 minutes; Nile blue at 60℃ for 20 minutes, followed by staining at room temperature for 20 minutes; and Sudan black B staining at 37℃ for 30 minutes. After staining, a drop of the sediment was placed on a glass slide. A coverslip was used, and stainability was observed under a microscope. Staining of mulberry bodies (cells) was compared with that of OFBs.

RESULTS

Appearance of Mulberry Bodies (Cells) After Sternheimer Staining

The results of Sternheimer staining are shown in **Figure 1**. The mulberry bodies (cells) exhibited various appearances (**Figures 2A** and **2B**). Differentiating mulberry bodies (cells) from fat granules and OFBs using Sternheimer's staining was difficult because they were small and closely resembled each other. The stainability of urine in these three patients did not differ.

Comparison of Four Fat Staining Methods

The results of fat staining, including Sudan III, Oil Red O, Nile blue, and Sudan black B, are shown in **Figure 3**. The colors of the OFBs obtained using each staining

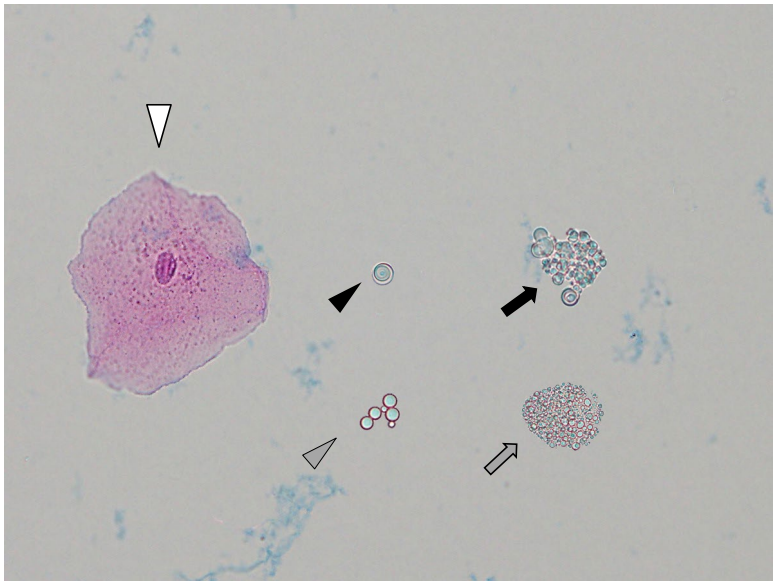

Figure 1 Comparison of mulberry bodies (cells) and other urinary sediment constituents using Sternheimer's staining (high-power field, 400×).
Mulberry bodies (black arrowhead), mulberry cells (black arrow), fatty granules (gray arrowhead), oval fat bodies (gray arrow), and squamous cells (white arrowhead).

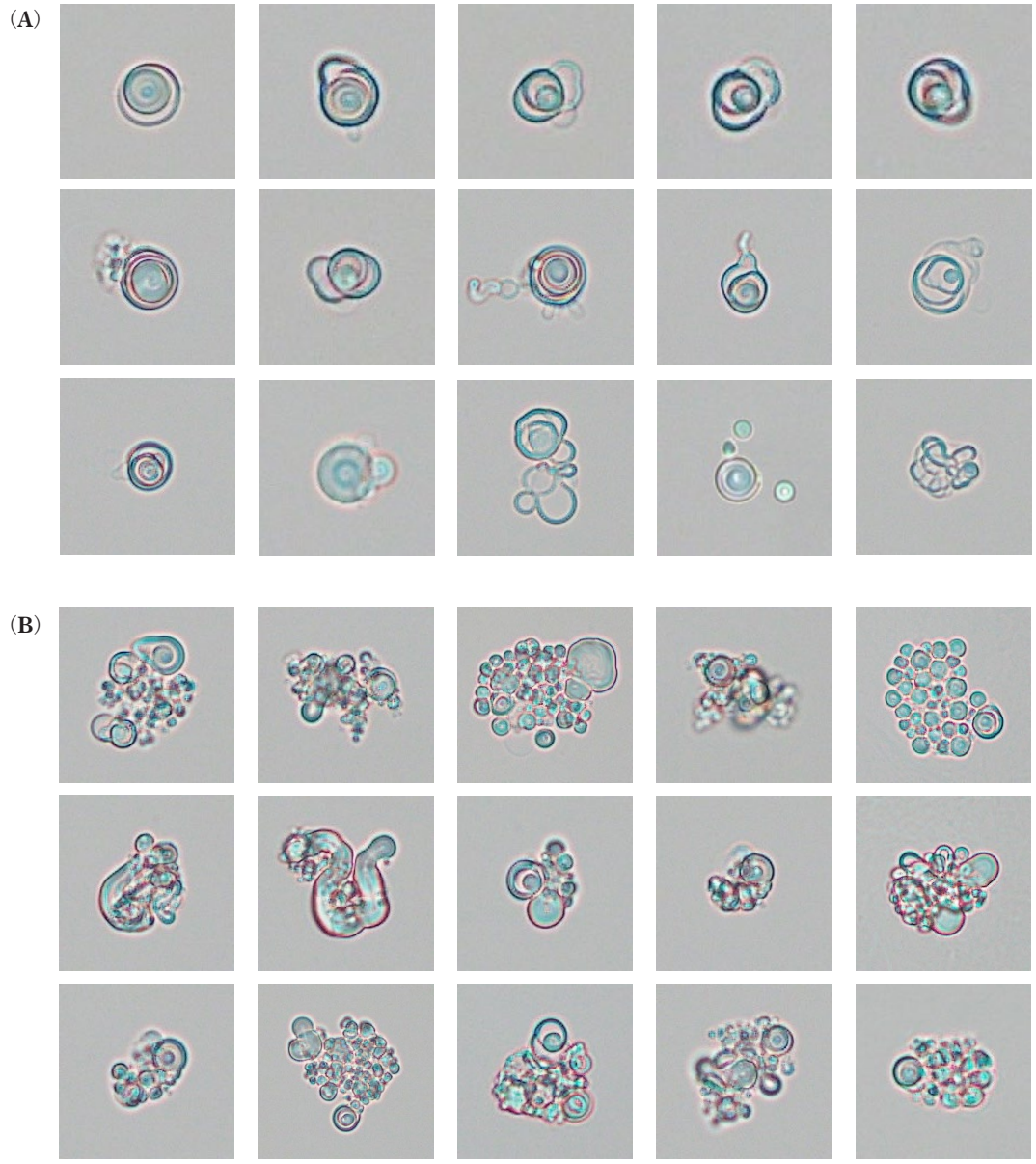

Figure 2 Appearance of mulberry bodies (cells) after Sternheimer's staining.
Mulberry bodies (**A**) and cells (**B**) showed different appearances. They resemble fatty granules and oval fat bodies, making differentiation difficult.

method were orange, brown, intense blue, and blue. Furthermore, the mulberry bodies (cells) appeared pale lemon yellow, pale red or unstained, or blue or black. The identification of mulberry bodies (cells) using Sudan III and Oil Red O staining was difficult; however, they were easily identifiable using Nile blue and Sudan black B staining. The staining results were consistent across the three patients.

As shown in **Figure 3** (**A**), differentiation between mulberry bodies (cells) and OFBs was challenging when using Sudan black B, as both exhibited a similar blue coloration. In contrast, Sudan III and Oil Red O staining produced more pronounced color differences between the two structures, aiding their distinction in routine microscopy (high-power fields). Furthermore, **Figure 3** (**B**) summarizes that Sudan III, Oil Red O, Nile blue and Sudan black B stainings were shown. Nile blue, Sudan black B yielded intense coloration of the mulberry bodies (cells), which facilitated their positive identification (**Table 1**).

DISCUSSION

Mulberry bodies (cells) are characteristically whorl-like in appearance [3)–6)]. However, their appearance varied, and staining mulberry bodies with Sudan III and Oil Red O was difficult. Sudan III and Oil Red O staining

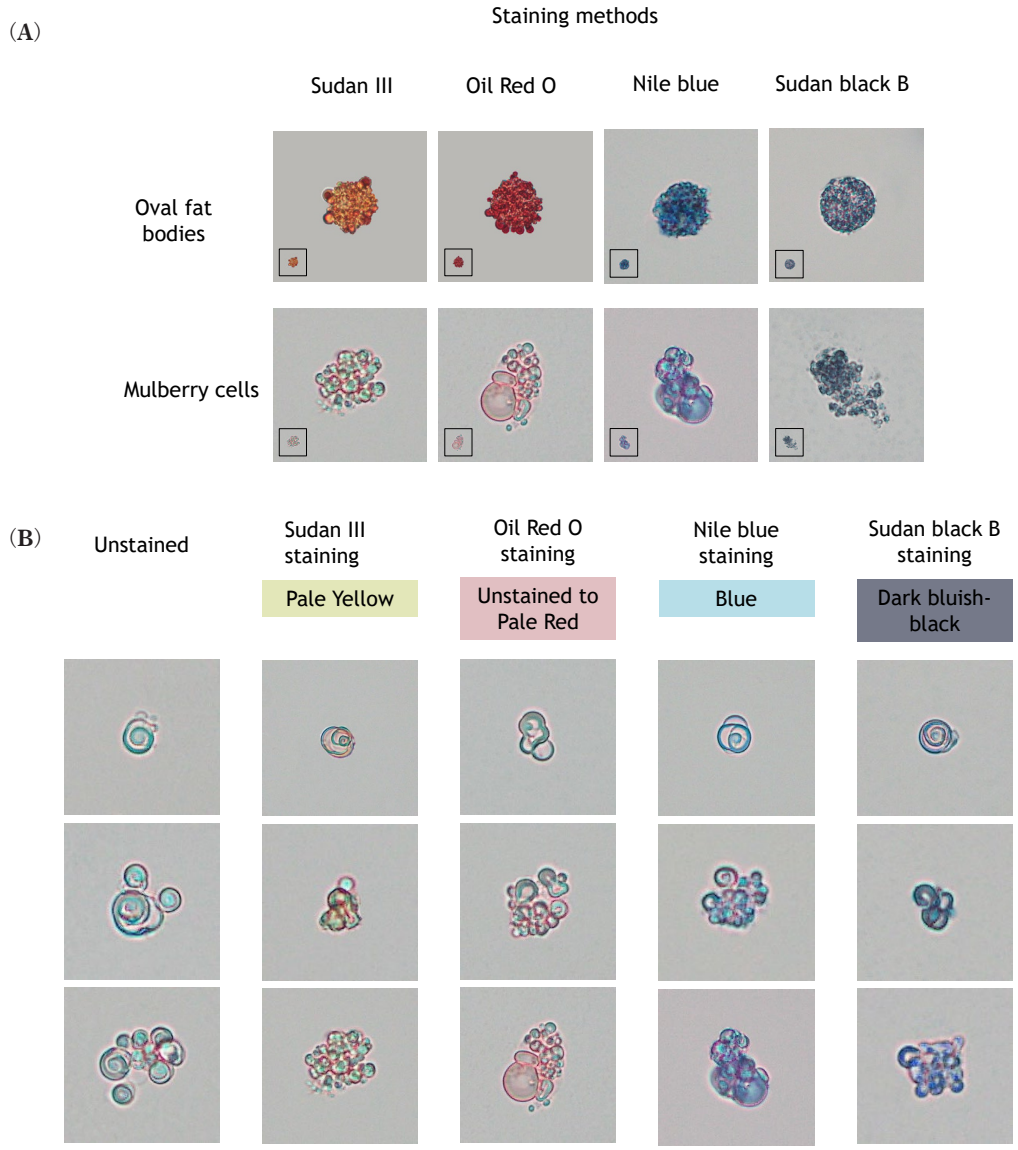

Figure 3 Comparison between oval fat bodies and mulberry cells.
The results of four types of fat staining are shown: Sudan III, Oil Red O, Nile blue, and Sudan black B. The colors of the oval fat bodies after fat staining were orange, brown, strongly blue, and blue (**A**). Mulberry bodies are approximately 8μm in size and extremely small. The lower left of Figure 3(**A**) shows mulberry cells under high-magnification microscopy. The mulberry cells were pale lemon-yellow, pale red, blue, and dark bluish-black. The oval fat bodies were stained orange to red with Sudan III and Oil Red O, whereas the mulberry bodies (cells) were weakly stained (**B**).

Table 1 Staining affinity of lipid-containing structures: mulberry bodies versus oval fat bodies.

Staining method	Structure	Staining characteristics	Lipid composition
Sudan III / Oil Red O	Mulberry bodies	Weakly stained or unstained	Globotriaosylceramide (GL-3)
	Oval fat bodies	Strongly stained	Triglycerides, Cholesterol esters
Nile Blue / Sudan black B	Mulberry bodies	Strongly stained	GL-3
	Oval fat bodies	Strongly stained	Triglycerides, Cholesterol esters

methods, which are often used for detecting OFBs in patients with nephrotic syndrome. As OFBs are composed of triglycerides and cholesterol esters, they are well stained with Sudan III and Oil Red O staining methods. In contrast, Nile blue and Sudan black B staining were more suitable for detecting mulberry bodies (cells) because they are composed of glycolipids. However, as illustrated in **Figure 3**(**A**), Sudan black B may not al-

ways be optimal for differentiating mulberry bodies from OFBs because both can show similar staining patterns. In such cases, Sudan III and Oil Red O, as demonstrated in **Figure 3**(**A**), offer clearer contrast for differentiation. Also, Nile blue as summarized in **Figure 3**(**A**)(**B**), was valuable for confirming the presence of mulberry bodies because of the intense and distinctive coloration of their glycolipid-rich structures. The colors of the oval fat bodies after fat staining were orange, brown, strongly blue, and blue (A). Mulberry bodies are approximately 8 μm in size and extremely small. The lower left of **Figure 3**(**A**) shows mulberry cells under high-magnification microscopy. The mulberry cells were pale-yellow, pale red, blue, and dark bluish-black. The oval fat bodies were stained orange to red with Sudan III and Oil Red O, whereas the mulberry bodies (cells) were weakly stained (B). Nile blue or Sudan black B staining following common fat staining (Sudan III or Oil Red O) facilitated the detection of mulberry bodies (cells). These morphological examination points are useful for improving the detection of mulberry bodies (cells) in laboratory practice. **Figures 3**(**A**) and (**B**) serve as visual guides summarizing the relative advantages of each staining method, offering a practical reference for laboratory technicians when encountering ambiguous lipid-containing structures in urinary sediments. Incorporating such a guide into routine diagnostic workflows may help reduce misidentification and improve the early detection of Fabry disease.

Conflict of Interest Statements

All authors declare that they have no conflicts of interest.

Funding Sources

No external or institutional funding was received for this study.

Acknowledgements

We express our gratitude to all our colleagues who supported our work at the Tokai University Hospital.

References

1) Meikle PJ, Hopwood JJ, Clague AE, et al. Prevalence of lysosomal storage disorders. JAMA. 1999; 281(3): 249-54. doi:10.1001/jama.281.3.249.
2) Germain DP. Fabry disease. Orphanet J Rare Dis. 2010; 5: 30. doi:10.1186/1750-1172-5-30.
3) Matsuura H, Asano K. Mulberry bodies: Fabry disease. Am J Med. 2018; 18(6): e111. doi:10.1016/j.amjmed.2018.04.030.
4) Shimohata H, Maruyama H, Miyamoto Y, et al. Urinary mulberry cells and bodies are useful tools for detecting late-onset Fabry disease. CEN Case Rep. 2017; 6: 148-51. doi:10.1007/s13730-017-0262-5.
5) Selvarajah M, Nicholls K, Hewitson TD, et al. Targeted urine microscopy for Anderson-Fabry disease: A cheap, sensitive, and specific diagnostic technique. Nephrol Dial Transplant. 2011; 26: 3195-202. doi:10.1093/ndt/gfr084.
6) Honda T, Komatsu E, Furuse S, et al. Fabry disease was diagnosed based on the presence of urinary mulberry bodies. Intern Med. 2016; 55(19): 2903. doi:10.2169/internalmedicine.55.7084.

Original

Optimizing Blood Collection and Storage Conditions for Soluble C-type Lectin-like Receptor 2 Measurement and Evaluating Diurnal Variation

Koichi Yamaguchi[*1,2§], Satomi Nagaya*[*2§], Asaka Matsui*[*3], Tomoki Togashi*[*2], Kota Iritani*[*4], Shoichi Sato*[*5], Masahide Kawamura*[*6], Shuhei Matsushita*[*7], Hiroaki Furuyama*[*7], Yoshitaka Yamaguchi*[*8], †Eriko Morishita*[*2,9]*

§ Equally contributed author

†Correspondence: Department of Clinical Laboratory Science, Division of Health Sciences, Graduate School of Medical Science, Kanazawa University, 5-11-80 Kodatsuno, Kanazawa, Ishikawa 920-0942, Japan
Tel: +81-76-265-2606; Fax: +81-76-265-2606;
E-mail: eriko86@staff.kanazawa-u.ac.jp
Received July 15, 2025; accepted November 10, 2025
*1 Department of Medical Technology, Faculty of Health Science, Tsukuba International University, 6-20 Manabe, Tsuchiura, Ibaraki 300-0051, Japan
*2 Department of Clinical Laboratory Science, Division of Health Sciences, Graduate School of Medical Science, Kanazawa University, 5-11-80 Kodatsuno, Kanazawa, Ishikawa 920-0942, Japan
*3 Asanogawa General Hospital, 83 Kosakamachinaka, Kanazawa, Ishikawa 920-8621, Japan
*4 Japanese Red Cross Aichi Medical Center Nagoya Daini Hospital, 2-9 Myoken-cho, Showa-ku, Nagoya, Aichi 466-8650, Japan
*5 Faculty of Medical Sciences, Juntendo University, Urayasu, Chiba 279-0021, Japan
*6 PHC Corporation, Scientific Marketing Department, In Vitro Diagnostic Division, Shimizu-cho, Itabashi-ku, Tokyo 174-0053, Japan
*7 PHC Corporation Reagent Development Group 2 Reagent Development Department Products Management Department In Vitro Diagnostic Division, Mitodai, Tako-machi, Katori-gun, Chiba 289-2247, Japan
*8 School of Health Science at Narita, International University of Health and Welfare, 4-3 Kozunomori, Narita-shi, Chiba 286-8686, Japan
*9 Department of Hematology, Kanazawa University Hospital, 13-1 Takaramachi, Kanazawa, Ishikawa 920-8640, Japan

ABSTRACT

Platelets play a central role in hemostasis and thrombosis, with excessive activation contributing to thrombotic disease. While conventional activation markers such as platelet factor 4 (PF4), β-thromboglobulin (β-TG), and glycoprotein VI (GPVI) are measurable by ELISA, their utility is limited by pre-analytical variability associated with factors such as exercise, smoking, caffeine intake, and sample handling. Soluble C-type lectin-like receptor 2 (sCLEC-2) has recently been identified as a novel biomarker released upon platelet activation, although its stability and physiological variation have not been fully elucidated.

sCLEC-2 was measured using an automated chemiluminescence immunoassay (STACIA®). Blood from healthy volunteers into 3.2% sodium citrate (4.5 mL) and EDTA (2.0 mL) tubes was centrifuged to separate plasma and then stored in tubes at room temperature or 4℃ for up to 24 hours. The influence of residual platelets on sCLEC-2 levels was evaluated. Diurnal variation was assessed in healthy volunteers, and correlations with GPVI were analyzed in 29 patients with hematologic disorders.

sCLEC-2 levels were 1.5-fold higher in EDTA samples than in citrate ($p < 0.05$). Immediately separated plasma remained stable for 24 hours, whereas storage in tubes led to time-dependent increases. Residual platelet counts above $1.0 \times 10^4/\mu L$ significantly elevated sCLEC-2. Morning sCLEC-2 levels were higher, consistent with the di-

urnal pattern of PAI-1. In hematologic disorders likely involving platelet activation, sCLEC-2 strongly correlated with GPVI ($r = 0.809$, $p < 0.001$). These findings demonstrate that sCLEC-2 is a sensitive and stable biomarker of platelet activation and provide practical recommendations for clinical sample handling.

〔Lab Med Int 2026; 5(1): 25-33〕

Key Words

Soluble C-type lectin-like receptor 2 (sCLEC-2), Activated platelets, Plasma assay, Sample stability, Sample storage conditions

INTRODUCTION

Traditionally, platelet factor 4 (PF4) and β-thromboglobulin (β-TG) measured by enzyme-linked immunosorbent assay (ELISA), as well as glycoprotein VI (GPVI), have been widely used to quantify platelet activation [1]. However, PF4 and β-TG levels are highly susceptible to pre-analytical factors such as exercise, smoking, caffeine intake, blood collection procedures, and sample handling, which complicates data interpretation. Unless these pre-analytical conditions are strictly controlled, the assessment of platelet activation becomes unstable and may lead to misinterpretation.

Recently, Kazama et al. developed soluble C-type lectin-like receptor 2 (sCLEC-2) as a novel biomarker of platelet activation [1]. CLEC-2 is a receptor expressed on the platelet membrane, and upon platelet activation, a portion is released into the plasma either as soluble fragments (shed CLEC-2) or as microparticle-associated CLEC-2 (MP-CLEC-2) [2]. Therefore, measurement of sCLEC-2 directly and quantitatively reflects platelet activation. Indeed, sCLEC-2 has been reported to be significantly elevated in thrombotic microangiopathy, disseminated intravascular coagulation [3)-5)], and acute coronary syndrome [2)6)], demonstrating its clinical utility. Moreover, in some cases of diabetes and atherosclerosis, sCLEC-2 has also been shown to be useful for evaluating platelet activation [1]. Thus, sCLEC-2 holds promise as a biomarker for the evaluation and diagnosis of various thrombotic disorders. Furthermore, sCLEC-2 can now be measured using an automated chemiluminescence immunoassay system (STACIA®, PHC Corporation, Tokyo, Japan), providing simple and reliable results comparable to those of routine coagulation assays [7]. According to Kazama et al. [1] and Ueda et al. [8], both sodium citrate and EDTA plasma are suitable for sCLEC-2 measurement, with no significant difference observed between them [1)8)]. However, since residual platelets can affect the measurement, appropriate centrifugation and sampling are essential [7)8)]. Additionally, when plasma is stored under refrigeration or frozen after separation, stable results can be obtained for up to 28 days [8]. Based on these findings, sCLEC-2 is considered feasible marker of platelet activation in routine clinical practice.

However, the studies by Kazama et al. [1] and Inoue et al. [2] primarily focused on fundamental investigations, such as the correlation between sCLEC-2 and GPVI, as well as the release mechanism of CLEC-2 during platelet activation, and thus did not directly address issues of specimen handling in routine clinical testing. Ueda et al. [8] and Kawamura et al. [7] analyzed pre-analytical factors, including anticoagulant type and residual platelets, in detail, thereby contributing to improved measurement reliability. Notably, in routine testing, immediate plasma separation after collection is not always feasible, and the stability of sCLEC-2 when whole blood is stored at room temperature or 4℃ remains unclear. Moreover, to apply sCLEC-2 as a platelet activation marker in clinical practice, it is essential to clarify its physiological variability, particularly whether diurnal variation exists. Therefore, verification of its stability under clinically relevant storage conditions, as well as assessment of physiological variability, is required to establish the clinical utility of sCLEC-2. Accordingly, in this study, we aimed to reproduce and expand upon previous basic findings, evaluate the stability of sCLEC-2 under storage conditions relevant to routine clinical practice, and investigate the diurnal variation of sCLEC-2 in healthy individuals.

MATERIALS AND METHODS

This study was conducted in accordance with the Declaration of Helsinki and was approved by the Ethics Committee of Kanazawa University (No. 981-3) and the Ethics Committee of Tsukuba International University (No. R05-8).

1. Sample Preparation and sCLEC-2 Measurement

Plasma samples that had been frozen at –80℃ were thawed in a 37℃ water bath for 5 minutes and used for sCLEC-2 measurement. The measurements were performed on the STACIA® (PHC Corporation, Tokyo, Japan) based on the chemiluminescent enzyme immunoassay (CLEIA). The assay kit employed anti-CLEC-2

monoclonal antibodies (11D5 and 11E6). The measurement procedure was as follows: plasma samples were incubated with magnetic particles coated with solid-phase anti-CLEC-2 monoclonal antibody (11D5). After washing, alkaline phosphatase–conjugated anti-CLEC-2 monoclonal antibody (11E6) was added and incubated. Following a second wash, the chemiluminescent substrate CDP-Star (Applied BioSystems, Waltham, MA) was added to induce luminescence, and the signal intensity was measured.

2. Evaluation of the Association Between Anticoagulants, Sample Storage Conditions, Residual Platelet Count, and sCLEC-2 Levels

2.1 Analysis of sCLEC-2 Levels by Anticoagulant Type

This study used samples from four healthy volunteers who provided informed consent: two males (32 ± 4 years) and two females (38 ± 11 years). Blood was drawn using a 21-gauge winged needle (Terumo Corporation, Tokyo, Japan). The blood collection tubes used were 3.2% sodium citrate tubes (4.5 mL), commonly used for coagulation tests (Becton, Dickinson and Company, Franklin Lakes, NJ), and EDTA tubes (2.0 mL), used for blood count tests (Becton, Dickinson and Company). Each tube was gently inverted 10 times after collection, followed by centrifugation at 2,000 × g for 15 minutes to separate the plasma, which was immediately frozen and stored at –80℃. Notably, although the recommended centrifugation conditions for coagulation testing samples are typically 1,500 × g for 15 minutes or 2,000 × g for 10 minutes, centrifugation at 2,000 × g for 15 minutes was to minimize the influence of residual platelets.

2.2 Analysis of the Effect of Sample Storage Conditions on sCLEC-2 Levels

The samples and blood collection methods used in this experiment were the same as those used in the study of anticoagulant types involving four healthy volunteers. To reflect routine clinical practice, the following storage conditions were established: (1) blood samples were centrifuged immediately after collection and then stored at room temperature or 4℃ in the original tubes; (2) blood samples were centrifuged immediately after collection, and the separated plasma was transferred to secondary tubes and stored at room temperature or 4℃. To evaluate time-dependent changes under each condition, plasma samples were taken at 0 hours (immediately after centrifugation), as well as at 1, 2, 4, 8, and 24 hours, from both the samples that were centrifuged immediately after blood collection and stored in the original tubes, and the separated tubes that had been stored. All samples were stored at –80℃ until measurement.

2.3 Relationship Between Residual Platelet Count in Plasma After Centrifugation and sCLEC-2 Levels

The samples and blood collection methods used in the experiment were the same as those used in the study of anticoagulant types involving four healthy volunteers. After blood collection, platelet-rich plasma (PRP) obtained by centrifugation at 200 × g for 10 minutes and platelet-poor plasma (PPP) obtained by centrifugation at 2,000 × g for 15 minutes were mixed, and the platelet count in the measurement samples was adjusted using an automated hematology analyzer, XN-300 (Sysmex, Kobe, Japan). The residual platelet counts in the measurement samples were adjusted to three levels: less than 1.0 × 10^4/μL, 1.0–2.9 × 10^4/μL, and 3.0–5.0 × 10^4/μL, and sCLEC-2 levels were measured for each. These three platelet count ranges were defined as group I (<1.0 × 10^4/μL), group II (1.0–2.9 × 10^4/μL), and group III (3.0–5.0 × 10^4/μL), respectively.

3. Evaluation of Diurnal Variation in Platelet Activation Using sCLEC-2

Blood samples were collected from seven healthy volunteers (three males, 32 ± 13 years; four females, 26 ± 6 years) using 3.2% sodium citrate tubes (4.5 mL). Blood collection was performed at 6:00, 12:00, and 18:00, and all collections were conducted after the participants had fasted for at least two hours prior to each time point. After centrifugation at 2,000 × g for 15 minutes, plasma was separated and frozen at –80 ℃ until sCLEC-2 measurement. Notably, plasminogen activator inhibitor-1 (PAI-1) has been reported to exhibit higher levels in the morning and lower levels in the afternoon. In this study, PAI-1 was measured as a positive control for the evaluating the diurnal variation in sCLEC-2[9)10)]. PAI-1 levels were measured using the LPIA tPAI test (PHC Corporation) on the STACIA® system.

4. Measurement of GPVI in Plasma from Patients with Hematologic Disorders and Its Correlation with sCLEC-2

To evaluate the correlation between GPVI and sCLEC-2, we analyzed samples from patients in whom high platelet activation was expected. The study included 29 patients (74 ± 12 years; 12 males, 17 females) from the Department of Hematology at Kanazawa University. The disease distribution of hematologic disorders was as follows: acute leukemia (2 cases), malignant lymphoma (11 cases), myelodysplastic syndrome (3 cases), multiple myeloma (4 cases), immune thrombocytopenia (3 cases), myeloproliferative neoplasm (1 case), and others (5 cases). Blood samples were collected using 3.2% sodium citrate tubes (4.5 mL). After centrifugation at 2,000

× g for 15 minutes, plasma was separated following routine coagulation testing and immediately frozen at –80℃ until measurement of sCLEC-2 and GPVI. All blood samples were collected in the morning. GPVI levels were measured using the Human GPVI ELISA Kit (Thermo Fisher Scientific Inc., Waltham, MA), according to the manufacturer's instructions.

5. Statistical Analysis

Graphs were generated using GraphPad Prism 10 (GraphPad Software, San Diego, CA), and statistical analyses were performed using StatFlex V7 (ver. 7, Medical Watch Institute, Ube, Japan). The Mann-Whitney test was used to compare sCLEC-2 levels by anticoagulant type. For comparisons based on sample storage conditions after blood collection, Dunn's test (multiple comparison vs. control group) was applied. sCLEC-2 and PAI-1 levels were expressed as median (minimum - maximum), whereas Age was expressed as mean ± SD. The association between GPVI and sCLEC-2 was evaluated using simple linear regression analysis. P-values < 0.05 were considered statistically significant.

RESULTS

1. Evaluation of Anticoagulants, Sample Storage Conditions, Residual Platelet Count, and Their Impact on sCLEC-2 Levels

1.1 Comparison of sCLEC-2 Levels by Anticoagulant Type

The sCLEC-2 levels by anticoagulant type were as follows: 3.2% sodium citrate (4.5 mL), 63.9 pg/mL (30.7–83.1); EDTA (2.0 mL), 94.2 pg/mL (66.3–118.2). The Mann-Whitney test revealed that sCLEC-2 levels in EDTA tubes were significantly higher than those in 3.2% sodium citrate tubes (**Fig. 1**, $p < 0.05$).

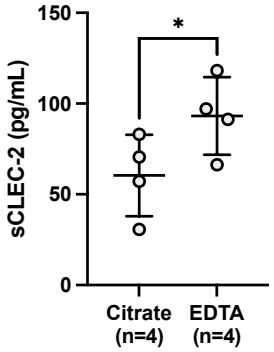

Figure 1 Comparison of sCLEC-2 levels in citrate or EDTA blood collection tubes
Comparison of sCLEC-2 levels based on the type of anticoagulant used. The anticoagulants compared were 3.2% sodium citrate (4.5 mL) and EDTA (2.0 mL). * $p < 0.05$.

1.2 Effect of Post-Centrifugation Storage in Original Blood Collection Tubes on sCLEC-2 Levels

sCLEC-2 levels were measured over time in two types of blood collection tubes, 3.2% sodium citrate (4.5 mL) and EDTA (2.0 mL), with samples stored at room temperature or 4 ℃ after centrifugation without plasma separation. In samples stored at room temperature in 3.2% sodium citrate tubes, a sharp increase in sCLEC-2 was observed only in Sample C after 8 hours; however, no statistically significant differences were observed up to 24 hours (**Fig. 2A**). In samples stored at 4 ℃ in 3.2% sodium citrate tubes, a significant increase in sCLEC-2 levels was observed at 24 hours (**Fig. 2B**, $p < 0.01$). In samples stored at room temperature in EDTA tubes, sCLEC-2 levels were significantly elevated at 24 hours (**Fig. 2C**, $p < 0.01$). In samples stored at 4℃ in EDTA tubes, sCLEC-2 levels showed a significant increase beginning at 8 hours (**Fig. 2D**; at 8 hours, $p < 0.05$; at 24 hours, $p < 0.01$).

1.3 Effect of Storage After Plasma Separation on sCLEC-2 Levels

Plasma was separated immediately after centrifugation and stored at room temperature or 4 ℃ , and sCLEC-2 levels were measured over time. In plasma samples from 3.2% sodium citrate tubes (4.5 mL), no statistically significant differences in sCLEC-2 levels were observed at either room temperature or 4℃ up to 24 hours (**Fig. 2E**, **F**). Similarly, in plasma samples collected using EDTA tubes (2.0 mL), no statistically significant differences were observed under either storage condition up to 24 hours (**Fig. 2G**, **H**).

1.4 Relationship Between Residual Platelet Count in Plasma and sCLEC-2 Levels

Blood samples from four volunteers (Sample A–D) were centrifuged, and the residual platelet count in plasma and sCLEC-2 levels were measured. The definitions of platelet count groups were as described in the Methods section. In sodium citrate tubes (4.5 mL), the sCLEC-2 levels were as follows: group I, 101.4 pg/mL (51.3–164.5); group II, 507.4 pg/mL (345.6–542.4); group III, 513.7 pg/mL (361.4–584.7). A significant increase in sCLEC-2 levels was observed in group III compared to group I (**Fig. 3A**, $p < 0.05$). Similarly, in EDTA tubes (2.0 mL), sCLEC-2 levels were as follows: group I, 93.7 pg/mL (58.9–100.1); group II, 161.3 pg/mL (145.7–209.6); group III, 1364.8 pg/mL (1110.0–1952.4). A significant increase in sCLEC-2 levels was also observed in group III compared to group I (**Fig. 3B**, $p < 0.05$).

2. Diurnal Variation in sCLEC-2 Levels

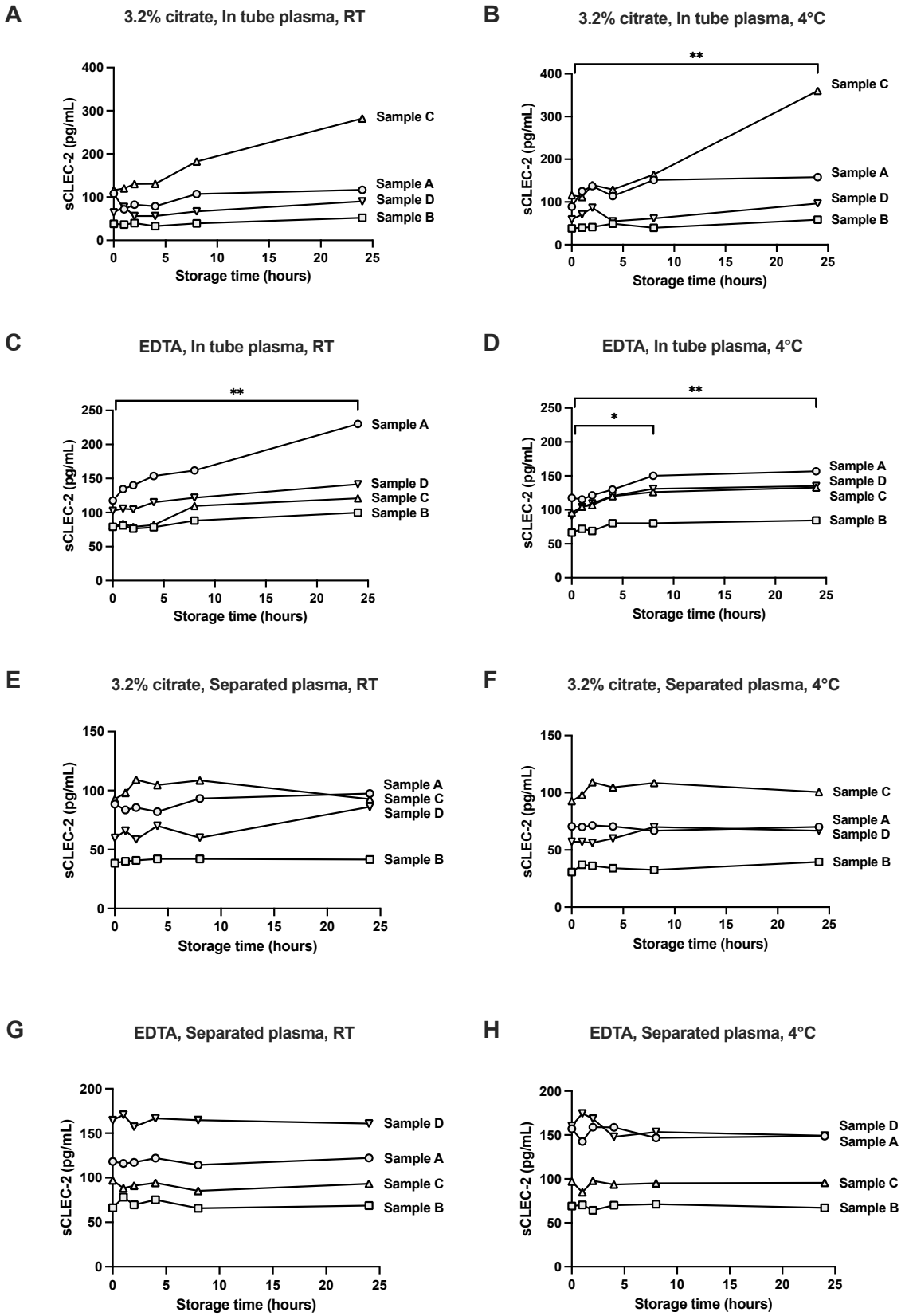

Figure 2 Effects of post-centrifugation storage in blood collection tubes and separated plasma, as well as storage temperature, on time-dependent changes in sCLEC-2 levels

Changes in sCLEC-2 levels in sodium citrate (A, B) and EDTA (C, D) blood collection tubes after centrifugation, with samples stored at room temperature (A, C) or 4℃ (B, D). Changes in sCLEC-2 levels in sodium citrate (E, F) and EDTA (G, H) plasma after centrifugation and plasma separation, with samples stored at room temperature (E, G) or 4℃ (F, H). * $p < 0.05$, ** $p < 0.01$.

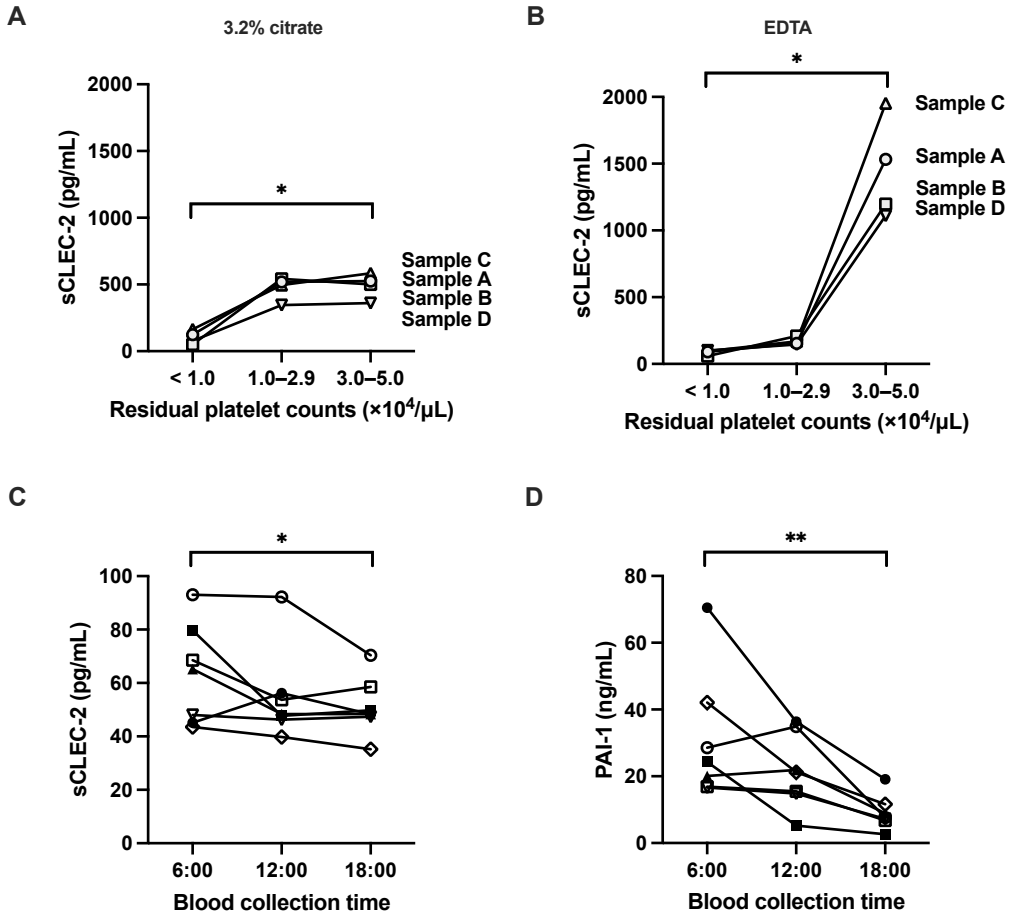

Figure 3 The relationship between residual platelet counts and sCLEC-2 levels, and the diurnal variation of sCLEC-2 and PAI-1

Residual platelet counts and sCLEC-2 levels are displayed according to anticoagulant type. (A) Sodium citrate tube and (B) EDTA tube. Diurnal variation of sCLEC-2 (C) and PAI-1 (D) levels in sodium citrate plasma is also presented. * $p < 0.05$, ** $p < 0.01$.

The diurnal variation of platelet activation was evaluated using sCLEC-2 levels in sodium citrate plasma. The sCLEC-2 levels were as follows: 65.2 pg/mL (43.5–93.0) at 6:00, 48.4 pg/mL (39.8–92.2) at 12:00 ($p = 0.1537$), and 48.4 pg/mL (35.2–70.4) at 18:00 ($p = 0.0414$), showing a statistically significant decrease at 18:00 compared with 6:00 (**Fig. 3C**). PAI-1 also demonstrated the expected diurnal variation, with levels of 24.3 ng/mL (16.6–70.5) at 6:00, 21.2 ng/mL (5.2–36.4) at 12:00 ($p = 0.8450$), and 7.6 ng/mL (2.7–19.1) at 18:00 ($p = 0.0027$), indicating a significant decrease at 18:00 compared with 6:00 (Fig. 3D).

3. Correlation Between GPVI and sCLEC-2 in Plasma of Patients with Hematologic Disorders

Sodium citrate plasma samples from 29 patients with hematologic disorders, in whom platelet activation was expected, were used to measure GPVI, a well-established marker of platelet activation , and sCLEC-2 levels. Simple linear regression analysis revealed a significant positive correlation between GPVI and sCLEC-2 (**Fig. 4**, $r = 0.809$, $p < 0.001$).

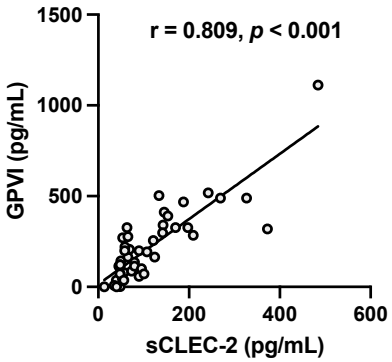

Figure 4 Correlation analysis of GPVI and sCLEC-2 levels

Correlation between GPVI and sCLEC-2 levels in sodium citrate plasma from patients with hematologic disorders.

DISCUSSION

In this study, we comprehensively evaluated the clinical utility of sCLEC-2 as a biomarker of platelet activation by investigating its analytical stability and reliability under pre-analytical conditions that reflect routine clinical practice. Specifically, we examined the effects of anticoagulant type, sample storage conditions, residual platelet count, and diurnal variation on sCLEC-2 measurement. In addition, we assessed the correlation between sCLEC-2 and GPVI, a conventional marker of platelet activation, in patients with hematologic disorders. These findings provide valuable insights into the applicability and limitations of sCLEC-2 in real-world clinical settings.

First, we examined the influence of anticoagulants on sCLEC-2 measurement under pre-analytical conditions. Our results demonstrated that sCLEC-2 levels in EDTA tubes (2.0 mL) were approximately 1.5 times higher than those in 3.2% sodium citrate tubes (4.5 mL). Ueda et al. [8] compared EDTA (2.0 mL), 3.2% sodium citrate (2.0 mL), and 3.2% sodium citrate (5.0 mL) tubes, reporting no difference between EDTA (2.0 mL) and 3.2% sodium citrate (2.0 mL), whereas a significant decrease was observed in 3.2% sodium citrate (5.0 mL) tubes compared with both. Although our study was limited to only four samples, which is insufficient to ensure statistical reliability, it is likely that the use of 4.5 mL sodium citrate tubes and the absence of dilution correction for citrate contributed to the lower sCLEC-2 levels observed compared with EDTA tubes. Furthermore, although plasma was carefully collected after centrifugation, strict control of the sampling position, such as maintaining a constant distance from the buffy coat, was not implemented. Therefore, the potential influence of tube volume and sampling depth on sCLEC-2 levels cannot be completely ruled out. Ueda et al. also investigated several pre-analytical factors, including centrifugal force and negative pressure differences among collection tubes [8]; however, the precise mechanisms remain unclear, and further investigation is warranted. For the clinical application of sCLEC-2, both EDTA and sodium citrate tubes appear to be feasible. Nevertheless, when platelet activation is assessed as part of hemostasis and thrombosis testing, or when consistency in pre-analytical processing is prioritized, the use of 2.0 mL 3.2% sodium citrate tubes may be preferable. However, further validation is needed to ensure its practical implementation in clinical laboratories.

It has been reported that arterial thrombosis, such as cerebral infarction and myocardial infarction, occurs more frequently in the early to late morning hours [11–15]. In this study, we evaluated the diurnal variation of sCLEC-2 in seven healthy volunteers and found that, in six out of seven participants, sCLEC-2 levels were higher in the morning and decreased toward the evening. This pattern was consistent with the known diurnal variation of PAI-1, and the sCLEC-2 level at 18:00 was significantly lower than that at 6:00 ($p < 0.01$). Although previous studies have reported that platelet activation tends to be higher in the morning [9,10], our results show a similar trend for sCLEC-2, further supporting the utility as a marker of platelet activation. These findings highlighted the importance of considering the timing of blood collection when clinically evaluating sCLEC-2 levels.

Blood samples used in clinical testing are typically stored at room temperature or refrigerated for a certain period to accommodate requests for retesting or additional analyses. Upon arrival at the laboratory, blood collected in EDTA tubes for complete blood count (CBC) testing is analyzed directly as whole blood. In contrast, blood collected in 3.2% sodium citrate tubes for coagulation testing is immediately centrifuged and used for coagulation assays, including prothrombin time (PT) and activated partial thromboplastin time (APTT). Ueda et al. investigated the stability of sCLEC-2 in plasma samples after centrifugation and separation, reporting that sCLEC-2 levels remained stable for up to 28 days [8]. In this study, in addition to evaluating plasma samples separated after centrifugation as described by Ueda et al., we also investigated the stability of sCLEC-2 levels in samples that were stored in the original blood collection tubes without plasma separation following centrifugation. Specifically, we evaluated the impact of storage time and temperature after centrifugation on sCLEC-2 levels, simulating a situation in which sCLEC-2 measurement is additionally requested as a marker of platelet activation following CBC (EDTA tube) or coagulation testing (3.2% sodium citrate tube). For both anticoagulants, stable results were observed when samples were stored at room temperature for up to 4 hours. However, under refrigerated conditions at 4℃, considerable individual variability was noted; two participants (Sample A and C) exhibited an increasing trend in sCLEC-2 levels after 2 hours of storage in the blood collection tube (**Fig. 2B**). It has been reported that refrigerated storage of samples can affect coagulation assays such as PT and APTT with prolonged storage [16]. This alteration is thought to result not only from decreased activity of coagulation factors but also from residual platelets present in the buffy coat. Although the precise mechanism remains unclear, studies have

shown that when platelets are stored at 4 ℃ , inhibitory signals that normally suppress platelet activation become attenuated, thereby inducing platelet activation [17]. Therefore, when samples are stored in blood collection tubes, progressive platelet activation may occur, potentially resulting in a time-dependent increase in sCLEC-2 levels. Therefore, in clinical applications, sCLEC-2 values measured from plasma stored in blood collection tubes under refrigerated conditions following routine testing should be interpreted with caution, as inter-individual variability may lead to artificially elevated results. On the other hand, in samples where plasma was separated after centrifugation, stable sCLELC2 levels were obtained for up to 24 hours, regardless of the anticoagulant used or whether the samples were stored at room temperature or under refrigerated conditions, consistent with the findings of Ueda et al. [8]. Depending on the operational protocols of the laboratory, promptly separating plasma following coagulation testing and storing it under refrigerated or frozen conditions may allow for accurate measurement of sCLEC-2 levels when additional testing is requested.

Kawamura et al. also investigated residual platelets and demonstrated that when the number of residual platelets in plasma is high, sCLEC-2 levels exhibit a positive bias [7]. In the present study, PRP was added to PPP to adjust the residual platelet count, and the effect on sCLEC-2 levels was evaluated. As shown in Fig. 3A and B, in both EDTA-anticoagulated and 3.2% sodium citrate-anticoagulated blood, sCLEC-2 levels increased with rising residual platelet counts. According to the literature, approximately 2,000 to 4,000 copies of CLEC-2 are present on the surface of platelet membranes [18], and minimizing the number of residual platelets in plasma is essential for accurate measurement of sCLEC-2. As demonstrated in both this study and the report by Kawamura et al. [7], samples with residual platelet counts ≥ $1.0 \times 10^4/\mu L$ showed higher sCLEC-2 levels compared to those with counts below this threshold. In coagulation testing, including PT and APTT, it is also recommended that the residual platelet count be less than $1.0 \times 10^4/\mu L$; therefore, applying the same threshold in sCLEC-2 measurement contributes to obtaining stable results. In this study, centrifugation at 2,000 × g for 15 minutes at room temperature was performed to minimize residual platelets in plasma. According to the consensus guidelines published by the Japanese Society for Laboratory Hematology (JSLH) regarding the handling of coagulation testing samples, centrifugation at 1,500 × g for 15 minutes or 2,000 × g for 10 minutes is recommended. Therefore, it is important for each facility to establish appropriate centrifugation protocols that consider residual platelet counts to ensure the accuracy of sCLEC-2 measurement.

We observed a strong positive correlation between sCLEC-2 and GPVI, a well-established marker of platelet activation ($r = 0.809$, $p < 0.001$). Although correlation analysis was not performed in healthy individuals due to the anticipated clustering of their values within the lower range, the present findings in patients with disease are consistent with those reported by Yamashita et al. [5], further supporting the utility of sCLEC-2 as a marker reflecting platelet activation.

CONCLUSION

sCLEC-2 enables the measurement of platelet activation levels using plasma samples without the need for special blood collection tubes, in contrast to well-established markers of platelet activation. In addition, stable measurement results were obtained using 3.2% sodium citrate blood, which is commonly used in routine coagulation testing, when stored at room temperature for at least 4 hours. Furthermore, sCLEC-2 levels exhibited diurnal variation, being higher in the morning and lower in the evening, indicating the timing of blood collection should be considered when interpreting results. This study confirmed that sCLEC-2 is a reliable marker of platelet activation and can be stably measured in routine laboratory conditions. Currently, sCLEC-2 can be measured using automated chemiluminescent immunoassay systems, with stable results achieved. However, standardization, particularly with regard to pre-analytical processing and the influence of residual platelets, remains necessary. In the future, sCLEC-2 is expected to be increasingly utilized as a clinically valuable marker of platelet activation, particularly in conditions associated with enhanced platelet activity.

Funding

This study was conducted with the support of a research grant from Tsukuba International University. The measurement of sCLEC-2 was outsourced to LSI Medience, a member of the PHC Corporation Group. This work was also supported by the Japan Ministry of Health, Labour and Welfare Research Program on Rare and Intractable Diseases to E.M. (JPMH23FC1022).

Acknowledgments

We would like to express our sincere gratitude to Hidenori Akiba (Beckman Coulter, Inc.) for providing the monoclonal antibodies used in the FCM analysis.

Conflict of Interest

M.K. and S.M. are employees of PHC Corporation. E.M. has received research funding from PHC Corporation. The other authors declare no conflicts of interest.

References

1) Kazama F, Nakamura J, Osada M, et al. Measurement of soluble C-type lectin-like receptor 2 in human plasma. Platelets. 2015; 26: 711-9. doi: 10.3109/09537104.2015.1021319.
2) Inoue O, Osada M, Nakamura J, et al. Soluble CLEC-2 is generated independently of ADAM10 and is increased in plasma in acute coronary syndrome: comparison with soluble GPVI, Int J Hematol. 2019; 110(3): 285-94. doi: 10.1007/s12185-019-02680-4.
3) Yamamoto A, Wada H, Tomida M, et al. Super formula for diagnosing disseminated intravascular coagulation using soluble C-type lectin-like receptor 2. Diagnostics 2023; 13 (13): 2299. doi: 10.3390/diagnostics13132299.
4) Yamamoto A, Wada H, Ichikawa Y, et al. Soluble C-type lectin-like receptor 2 is a biomarker for disseminated intravascular coagulation. J Clin Med. 2021; 10(13): 2860. doi: 10.3390/jcm10132860.
5) Yamashita Y, Suzuki K, Matsumoto T, et al. Elevated plasma levels of soluble C-type lectin-like receptor 2 (CLEC-2) in patients with thrombotic microangiopathy, Thromb Res. 2019; 178: 54-8. doi: 10.1016/j.thromres.2019.03.018.
6) Nishigaki A, Ichikawa Y, Ezaki M, et al. Soluble C-type lectin-like receptor 2 elevation in patients with acute cerebral infarction. J Clin Med. 2021; 10 (15): 3408. doi: org/10.3390/jcm10153408.
7) Kawamura M, Ueda M, Matsushita S, et al. Development of an automated chemiluminescence enzyme immunoassay for the measurement of soluble C-type lectin-like receptor 2 (sCLEC-2) and molecular forms of sCLEC-2 measured in patient plasma. Platelets. 2024; 35(1): 2420949. doi: org/10.1080/09537104.2024.2420949.
8) Ueda M, Kazama F, Oishi S, et al. Measurement of soluble C-type lectin-like receptor 2. Jpn J Lab Hematol. 2024; 25(2): 251-8. (in Japanese).
9) Budkowska M, Lebiecka A, Marcinowska Z, et al. The circadian rhythm of selected parameters of the hemostasis system in healthy people. Thromb Res. 2019; 182: 79-88. doi: 10.1016/j.thromres.2019.08.015.
10) Scheer FA, Shea SA. Human circadian system causes a morning peak in prothrombotic plasminogen activator inhibitor-1 (PAI-1) independent of the sleep/wake cycle. Blood. 2014; 123(4): 590-3. doi: 10.1182/blood-2013-07-517060.
11) Mitrovic P, Stefanovic B, Vasiljevic Z, et al. The timing of infarction pain in patients with acute myocardial infarction after previous revascularization, Sci World J. 2008; 8: 598-603. doi: 10.1100/tsw.2008.88.
12) Omama S, Yoshida Y, Ogawa A, et al. Differences in circadian variation of cerebral infarction, intracerebral haemorrhage and subarachnoid haemorrhage by situation at onset, J Neurol Neurosurg Psychiatry. 2006: 77(12): 1345-9. doi: 10.1136/jnnp.2006.090373.
13) Li C, Li Y. Characteristics of onset seasons within one year and time periods within one day of acute myocardial infarction. Altern Ther Health Med. 2023; 29(3): 200-6.
14) Thompson DR, Blandford RL, Sutton TW, et al. Time of onset of chest pain in acute myocardial infarction, Int J Cardiol. 1985; 7(2): 139-48. doi: 10.1016/0167-5273(85)90354-7.
15) Goldberg RJ, Brady P, Muller JE, et al. Time of onset of symptoms of acute myocardial infarction. Am J Cardiol. 1990; 66(2): 140-4. doi: 10.1016/0002-9149(90)90577-n.
16) Baker P, Platton S, Gibson, C et al. Guidelines on the laboratory aspects of assays used in haemostasis and thrombosis. Br J Haematol. 2020; 191(3): 347-62. doi: 10.1111/bjh.16776.
17) Kobsar A, Koehnlechner K, Klingler P, et al. The effect of short-term refrigeration on platelet responsiveness. Sci Rep. 2022; 12(1): 16910. doi: 10.1038/s41598-022-21124-4.
18) Rayes J, Watson SP, Nieswandt B. Functional significance of the platelet immune receptors GPVI and CLEC-2. J Clin Invest. 2019; 129(1): 12-23. doi: 10.1172/JCI122955.
19) Ieko M, Komiyama Y, Yamazaki S, et al. Expert consensus regarding standardization of sample preparation for clotting time assays. Int J Hematol. 2020; 112(2): 614-20. doi: 10.1007/s12185-020-02983-x.

Original

Serum MMP-3 as a predictive factor for joint destruction in patients with rheumatoid arthritis who have achieved remission or low disease activity and the clinically relevant cut-off value for the structural remission

†Hiroe Konishi[*1], Mai Morimoto*[*1], Kosaku Murakami*[*2], Akira Onishi*[*3],*
Takayuki Fujii[*3,4], Koichi Murata*[*3,4], Masao Tanaka*[*3],*
Akio Morinobu[*5], Masayoshi Nakano*[*1,6], Masahiro Koshiba*[*1,7]*

†Department of Clinical Diagnosis and Laboratory Medicine, Hyogo Medical University School of Medicine, 1-1 Mukogawa-cho, Nishinomiya, Hyogo, 663-8501, Japan
Tel: +81-798-45-6860 Ex. 2450; Fax: +81-798-45-6873;
E-mail: hiroe-k@hyo-med.ac.jp
Received October 30, 2025; accepted December 11, 2025
*1 Department of Clinical Diagnosis and Laboratory Medicine, Hyogo Medical University School of Medicine, 1-1 Mukogawa-cho, Nishinomiya, Hyogo, 663-8501, Japan
*2 Division of Clinical Immunology and Cancer Immunotherapy, Center for Cancer Immunotherapy and Immunobiology, Kyoto University Graduate School of Medicine, Sakyo, Kyoto, 606-8501, Japan
*3 Department of Advanced Medicine for Rheumatic Diseases, Kyoto University Graduate School of Medicine, 54 Shogoin-Kawahara-cho, Sakyo, Kyoto, 606-8507, Japan
*4 Department of Orthopaedic Surgery, Kyoto University Graduate School of Medicine, Sakyo, Kyoto, 606-8507, Japan
*5 Department of Rheumatology and Clinical Immunology, Kyoto University Graduate School of Medicine, Sakyo, Kyoto, 606-8507, Japan
*6 Clinical Laboratory Department, Baba Memorial Hospital, 4-244 Hamadera Funao-cho Higashi, Sakai, Osaka, 592-8341, Japan
*7 Shinsuma Clinic, 5-1-4 Suma-Murasame-cho, Kobe, Hyogo, 654-0046, Japan

ABSTRACT

Objectives

Joint destruction progression is often seen in RA patients achieving low disease activity (LDA) or clinical remission. In this study we evaluated whether increased MMP-3 (including prednisolone-induced elevation) is relevant to the joint destruction progression, and to explore the best cut-off value for the structural remission.

Methods

RA patients whose CRP levels normalized following methotrexate (MTX) monotherapy or DMARD combination therapy (MTX together with other DMARDs) were divided into two groups based on their MMP-3 positivity at the end of 1-year observation period, and joint destruction progression was retrospectively compared. Radiological joint destruction was assessed using the modified van der Heijde total sharp score (mTSS). The cut-off value of MMP-3 was determined by ROC analysis.

Results

Among MMP-3 positive patients who have achieved DAS28-ESR LDA or clinical remission, joint destruction progressed in 50.0% of prednisolone(-) and 45.7% of prednisolone(+) patients (p=1.00). Similarly, among MMP-3 positive patients who have achieved CDAI LDA or clinical remission, joint destruction progressed in 48.3% of

prednisolone(-) and 42.6% of prednisolone(+) patients (p=0.79). The ROC analysis in female patients revealed that the cut-off value of MMP-3 was 49.7 ng/mL (AUC 0.681; 95% CI 0.560–0.802, p<0.01) for the structural remission (ΔmTSS<0.5).

Conclusions

The data presented here suggest that prednisolone-induced serum MMP-3 increase contribute similarly to the joint destruction compared with the MMP-3 increase without prednisolone. Also indicated is that the current cut-off value of serum MMP-3 (59.7 ng/mL) is too high to achieve the structural remission in female RA patients.

〔Lab Med Int 2026; 5(1): 34-45〕

Key Words

C-reactive protein, joint destruction, matrix metalloproteinase-3, modified van der Heijde total sharp score, Rheumatoid arthritis

I. INTRODUCTION

Rheumatoid arthritis (RA) is a systemic autoimmune disease characterized by chronic synovitis and joint destruction, which leads to disability [1]. Clinical remission is the current therapeutic target for patients with RA, with low disease activity (LDA) considered the best possible alternative. A targeted treatment strategy should be employed when treating patients with RA, and treatment decisions should then be based on disease activity and other patient factors, such as comorbidities and the progression of structural damage [2)3)].

Methotrexate (MTX) is recommended as the first-line drug for the initial treatment of RA and remains the anchor drug in RA [4)5)]. MTX is not only an efficacious conventional synthetic (cs) disease-modifying antirheumatic drug (DMARD), it is also the basis for combination therapies with prednisolone (PSL), other csDMARDs, biological DMARDs (bDMARDs) or targeted synthetic DMARDs (tsDMARDs) [6]. While serum CRP levels often normalize (i.e. below the upper reference limit) after MTX therapy, joint destruction can still progress [7].

Matrix metalloproteinases (MMPs) are a family of enzymes that catalyze extracellular matrix degradation. Most MMPs are secreted as inactive preproteins that are activated when cleaved by extracellular proteinases [8]. MMP-3 is a proteinase secreted by synovial fibroblasts and chondrocytes within joints. In RA, joint destruction can be accelerated by active MMP-3, and the level of MMP-3 is elevated within the joints of RA patients [9]. This high MMP-3 level is believed to mediate the joint destruction seen in patients with RA [10)11)].

Increases in serum MMP-3 levels are observed from early to advanced stages in 80% 90% of patients with RA. Serum MMP-3 levels in these patients reflect the degree of synovial cell proliferation and may serve as a prognostic indicator of RA progression, particularly early after disease onset [12)]. Elevated or increasing serum MMP-3 levels in patients with RA are associated with rapid progression of joint destruction while, conversely, serum MMP-3 levels decline when the condition stabilizes in response to the therapeutic effect of DMARDs [13)]. Normal serum MMP-3 levels in combination with decreases in CRP levels or disease activity are reportedly useful for predicting clinical remission and normal physical function in patients with RA [14)]. However, progression of joint destruction is often seen in RA patients who are in remission or exhibiting LDA and normalized CRP levels [15)]. Those reports prompted us to observe RA patients with normalized CRP levels for 1 year by MTX monotherapy or combination therapy (MTX together with other DMARDs) to determine whether serum MMP-3 positivity correlates with joint destruction on these patients. Oral prednisolone administration reportedly increases serum MMP-3 levels [16)17)]. Currently, however, there are no reports examining whether PSL-induced elevation of serum MMP-3 is involved in joint destruction, which also made us to evaluate whether PSL-induced elevation of serum MMP-3 is truly associated with the progression of joint destruction. The data also enabled us to propose an adequate cut-off value for MMP-3 based on the relationship between serum MMP-3 levels and joint destruction by ROC analysis.

II. METHODS

1. Study design and patient selection

Enrolled in the study were patients who visited Hyogo College of Medicine Hospital (currently Hyogo Medical University Hospital) or Kyoto University Hospital between April 2011 and April 2021 and met the 1987 and/or 2010 RA classification criteria. Patients with RA (n = 182) whose CRP levels normalized following MTX monotherapy or DMARD combination therapy (MTX together with other DMARDs) were divided into two

groups based on their MMP-3 positivity at the end of the 1-year observation period, and progression of joint destruction was retrospectively compared using X-rays.

2. Assessment

The medical records of the patients were retrospectively reviewed, including information related to their visual analog scale (VAS), CRP, erythrocyte sedimentation rate (ESR), rheumatoid factor (RF), serum MMP-3, anticitrullinated protein antibody (ACPA), 28 joint disease activity score (DAS28), and clinical disease activity index (CDAI). Patients who had severe renal dysfunction (eGFRcre < 30 mL/min/1.73 m^2), a contraindication to MTX administration, or were taking oral PSL > 25 mg/day due to complications were excluded. Patients with other forms of arthritis, such as ankylosing spondylitis, were also excluded because of their possible effect on MMP-3 levels. After the observation period, the patients were divided into MMP-3 positive (MMP-3(+)) and MMP-3 negative (MMP-3(−)) groups based on whether their MMP-3 levels were above or below the upper reference limit for each sex. Progression was assessed based on radiography of the hands, wrists and feet, and scored using the modified total sharp score (mTSS) method recommended by Bruynesteyn et al. (18). Radiographs of each patient's hands and feet were taken upon initiation of MTX therapy and after 1 year of therapy. Radiographic progression was evaluated independently by two rheumatologists (MM and KMurakami) trained on the mTSS scoring system and certified by Prof. van der Heijde (Leiden University). mTSS progression after 1 year (ΔmTSS) was then calculated from the mean progression determined by the two readers. If their calculations of ΔmTSS differed by ≥ 10, the two rheumatologists discussed the scores and reached a consensus. Patients were classified as exhibiting structural remission (ΔmTSS < 0.5) or radiographic evidence of progression (ΔmTSS ≥ 0.5).

3. Ethical approval

This study protocol was approved by the Ethics Committee of Hyogo Medical University (Protocol No. 3923). Because of the retrospective nature of the study, the requirement for individual informed consent was waived owing to the "opt-out" principle; that is, patients were allowed to "opt-out" of the database if they wanted. Use of clinical data collected at Kyoto University Hospital was approved by the Medical Ethics Committee of the Kyoto University Graduate School and Faculty of Medicine (No. R0357). Written informed consent to participate in the study was obtained from all patients treated at Kyoto University Hospital. This study was performed in accordance with the Declaration of Helsinki.

4. Statistical analysis

All statistical analyses were performed using IBM SPSS Statistics version 29 (IBM Corp., Armonk, NY, USA). Demographic and baseline characteristics were analyzed using Fisher's exact test for categorical variables and the Mann-Whitney U test for continuous variables. Multivariate analysis was performed using multiple logistic regression analysis with variables for which the p values were <0.05 in the preceding univariate analysis. All reported p values are two-sided and not adjusted for multiple testing. Any difference with a p value <0.05 was considered statistically significant.

III. RESULTS

1. Clinical characteristics of patients upon initiation of MTX therapy

Of the patients who received MTX monotherapy or DMARD combination therapy for at least 1 year, 182 (including 142 females) were evaluated radiographically. Upon initiation of MTX therapy (at baseline), participants had median age was 60 years (interquartile range [IQR], 51–68 years), with median disease duration was 6 years (IQR 3–11 years). Among them, 62.7% were RF-positive, 64.3% were ACPA-positive and 56.0% were both RF- and ACPA-positive. The median DAS28-ESR was 2.56 (IQR 1.94–3.21), the median CDAI was 3.50 (IQR 1.15–6.65), the median MTX dose was 6.0 mg/week (IQR 4.0–8.0 mg/week) in 125 (68.7%) patients, and the median PSL dose was 4.0 mg/day (IQR 2.0–5.0 mg/day) in 69 patients (37.9%) (**Table 1**).

Table 1 Subject demographics and clinical characteristics at 0week

Parameter	
Patients, n	182
Age (year, median, IQR)	60 (51-68)
Female, n (%)	142 (78.0)
RA duration (year, median, IQR)	6 (3-11)
RF positive (%)	62.7
ACPA positive (%)	64.3
RF & ACPA positive (%)	56.0
DAS28 (ESR) (median, IQR)	2.56 (1.94-3.21)
CDAI (median, IQR)	3.50 (1.15-6.65)
MTX use at baseline, n (%)	125 (68.7)
MTX dose (mg/w, median, IQR)	6 (4-8)
PSL use at baseline, n (%)	69 (37.9)

RA, rheumatoid arthritis; RF, rheumatoid factor; ACPA, anti-cyclic citrullinated peptide antibodies; DAS28, Disease Activity Score 28-joint assessment; CDAI, Clinical Disease Activity Index; MTX, methotrexate; PSL, prednisolone.

2. Comparison of joint destruction progression at the end of the 1-year observation period

The clinical characteristics of the joint destruction(−) group (n = 124) and joint destruction(+) group (n = 58) are summarized in **Table 2**. The numbers of serum MMP 3(+) patients in the joint destruction(−) and joint destruction(+) groups were 47 (37.9%) and 35 (60.3%), respectively. The median DAS28-ESR were 2.25 (IQR 1.75–2.89) and 2.51 (IQR 2.11–3.01), the median CDAI were 2.10 (IQR 0.70–5.88) and 3.20 (IQR 1.35–6.10), and the PSL usage rates were 33.9% (n = 42) and 39.3% (n = 22), respectively. There were no significant differences in disease activity or PSL usage rates between the joint destruction(−) and the joint destruction(+) groups. However, there were significant differences in gender, ACPA positivity, and MMP-3 positivity between the joint destruction(−) and the joint destruction(+) groups. We performed multivariate logistic regression analysis on these factors. The results showed that only MMP-3 positivity (odds ratio, 2.20; 95% CI: 1.14–4.25, p = 0.018) was significantly associated with joint destruction.

3. Comparison of progression of joint damage in MMP-3(−) and MMP-3(+) patients

The incidences of progression of joint destruction in MMP-3(−) (n = 100) and MMP-3(+) patients (n = 82) were 23.0% (n = 23) and 42.7% (n = 35), respectively (p < 0.01). The mean changes in the mTSS from baseline (ΔmTSS) were 0.46 ± 1.12 and 0.97 ± 1.99 (p = 0.03) (**Figure 1A**), and the incidences of nonprogression (ΔmTSS < 0.5) were 77.0% and 57.3% (**Figure 1B**). At baseline, the median MMP-3 levels were 55.0 ng/ml (IQR 44.2–84.6) and 119.0 ng/ml (IQR 78.0–159.6) (p < 0.01) and the PSL usage rates were 17.0% (n = 17) and 57.3% (n = 47) (p < 0.01). Progression of joint destruction was then further examined in the MMP-3(−) (n = 77) and MMP-3(+) (n = 36) patients not receiving PSL to exclude the effect of PSL for the serum MMP-3 increase. Among those patients, the incidences of joint destruction progression were 24.7% (n = 19) and 47.2% (n = 17) in the MMP-3(−) and MMP-3(+) groups, respectively (p = 0.03). The ΔmTSS values were 0.51 ± 1.22 and 1.03 ± 1.90 (p = 0.09) (**Figure 1C**), and the incidences of nonprogression were 75.3% and 52.8% (**Figure 1D**).

Notably, however, even when CRP levels had normalized after a year of treatment, it did not necessarily indicate the absence of inflammation. We sometimes encountered patients with a few small joint swellings but normalized CRP levels. We therefore assessed the progression of joint destruction in the MMP-3(−) (n = 58) and MMP-3(+) (n = 39) patients who exhibited no joint swelling at 1 year. Among this group, the incidences of joint destruction progression were 20.7% (n = 12) and 43.6% (n = 17) in the MMP-3(−) and MMP-3(+) patients, respectively (p = 0.02). The ΔmTSS values were

Table 2 Joint destruction (-) or (+) groups analysis at 1-year

	Joint destruction	Joint destruction		Multivariate	
	(-)	(+)	*p*	OR (95% CI)	*p*
Age (year, median, IQR)	60 (50-67)	61 (53-69)	0.4		
Female / Male	91 / 33	51 / 7	0.03	2.32 (0.94-5.71)	0.0681
RA duration (year, median, IQR)	6 (3-11)	6 (3-13)	0.25		
RF positive (%)	61.9	76.5	0.07		
ACPA positive (%)	57.9	77.8	0.04	1.44 (0.75-2.79)	0.2753
RF & ACPA positive (%)	51.4	65.7	0.22		
MMP-3 (+) group, n (%)	47 (37.9)	35 (60.3)	< 0.01	2.20 (1.14-4.25)	0.0182
DAS28 (ESR) (median, IQR)	2.25 (1.75-2.89)	2.51 (2.11-3.01)	0.17		
CDAI (median, IQR)	2.10 (0.70-5.88)	3.20 (1.35-6.10)	0.97		
MTX use, n (%)	104 (83.9)	45 (77.6)	0.31		
MTX dose (mg/w, median, IQR)	6 (4.5-8)	6 (6-10)	0.34		
PSL use, n (%)	42 (33.9)	22 (39.3)	0.61		
PSL dose (mg, median, IQR)	4 (2-5)	3 (2-5)	0.48		

Data are median (IQR).
RA, rheumatoid arthritis; RF, rheumatoid factor; ACPA, anti-cyclic citrullinated peptide antibodies; MMP-3, matrix metalloproteinase-3; DAS28, Disease Activity Score 28-joint assessment; CDAI, Clinical Disease Activity Index; MTX, methotrexate; PSL, prednisolone.

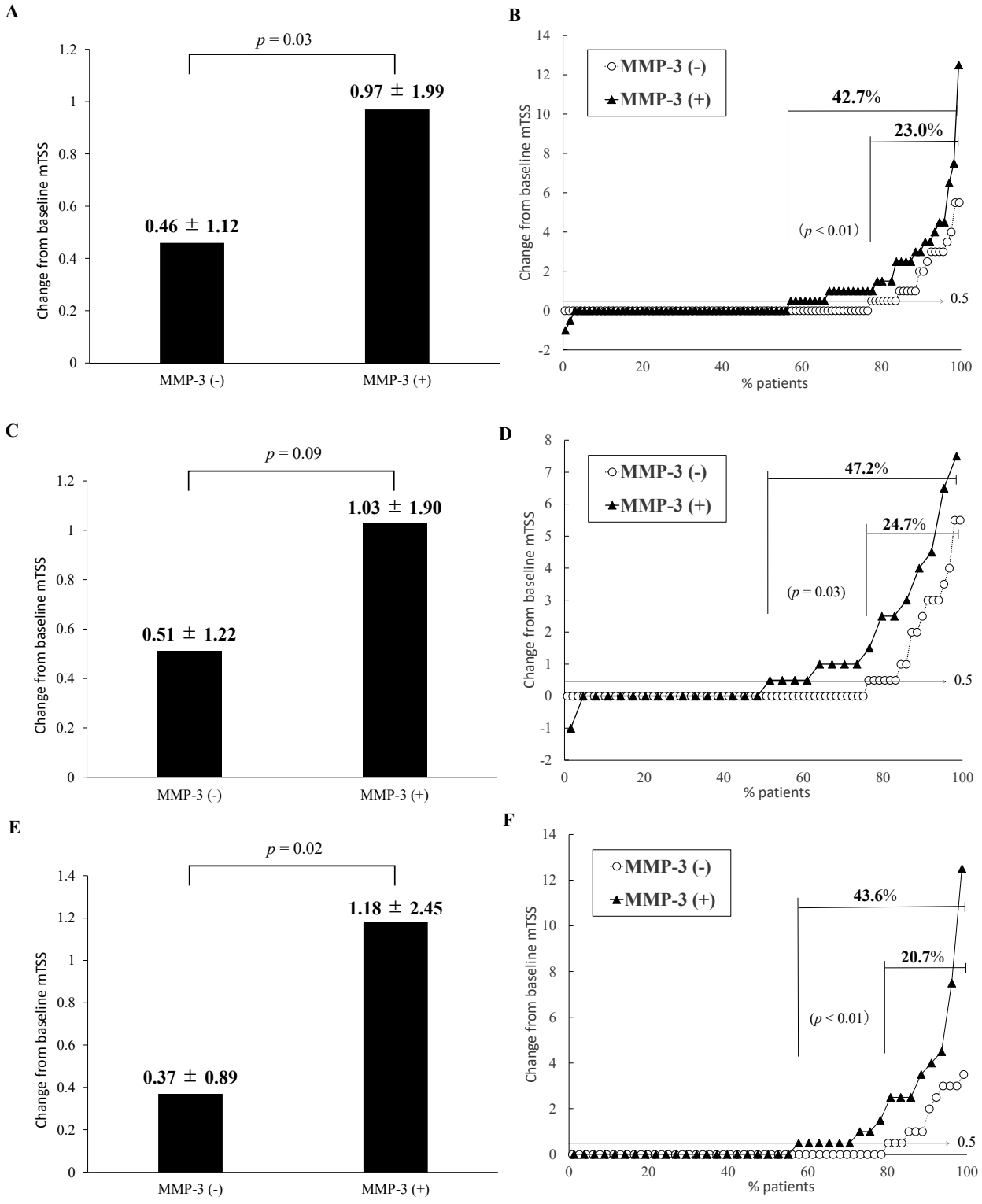

Figure 1 Progression of joint destruction in the MMP-3(−) and MMP-3(+) patients with RA after 1 year of treatment (A, B) Changes in the modified total sharp score from baseline (ΔmTSS) (A) and plot of cumulative mTSS probability (B) for the total RA patient sample (n = 182). (C, D) ΔmTSS (C) and cumulative mTSS probability (D) for RA patients not receiving PSL (n = 113). (E, F) ΔmTSS (E) and cumulative mTSS probability (F) for patients without swollen joints at 1 year (n = 97). Values in (A) (C) (E) indicate the mean (SD) at each time point and in the MMP-3(−) or MMP-3(+) group. Percentages in (B) (D) (F) indicate incidences of joint destruction progression (ΔmTSS > 0.5) in the MMP-3(−) or MMP-3(+) group.

0.37 ± 0.89 and 1.18 ± 2.45 (p = 0.02) (**Figure 1E**), the incidences of nonprogression were 79.3% and 56.4% (**Figure 1F**), and the PSL usage rates at baseline were 15.5% (n = 9) and 48.7% (n = 19) (p < 0.01) (**Table 3**).

4. Comparison of joint destruction progression between MMP-3(−) and MMP-3(+) patients with normal CRP levels at baseline

We also examined the progression of joint destruction in the 142 RA patients (MMP 3(−), n = 79; MMP-3(+), n = 63) who had normal CRP levels at baseline. Progression of joint destruction was detected in 24.1% (n = 19) and 47.6% (n = 30) (p < 0.01) of the MMP 3(−) and MMP 3(+) patents, respectively, while the ΔmTSS values were 0.47 ± 1.17 and 1.13 ± 2.21 (p = 0.03), the incidences of nonprogression (ΔmTSS < 0.5) were 75.9% and 52.4%, and the PSL usage rates at baseline were 15.2% (n = 12) and 57.1% (n = 36) (p < 0.01). This suggests that progression of joint destruction is more likely when MMP-3 levels remain positive, even when baseline CRP is normal.

5. Comparison of the progression of joint damage estimated by radiography in the MMP-3(−) and MMP-3(+) groups with LDA or clinical remission (DAS28-ESR < 2.6 or CDAI ≦ 2.8)

Clinical remission is the therapeutic target for patients with RA, with LDA being the best possible alternative. Thus, the study enrolled 109 of 183 patients with RA (MMP-3(−), n = 63; MMP-3(+), n = 46) who had achieved LDA or clinical remission (DAS28-ESR < 2.6). The progression of joint destruction was found in 25.4% (MMP-3(−)) and 50.0% (MMP-3(+)) (p < 0.01); the ΔmTSS values were 0.42 ± 1.02 and 1.21 ± 2.41 (p = 0.02); and the nonprogression rates (ΔmTSS < 0.5) were 74.6% and 50.0%, respectively. The progression of joint destruction was further examined in 70 of these 109 patients (MMP-3(−), n = 48; MMP-3(+), n = 22)

Table 3 MMP-3 (−) or (+) patients analysis at 1-year

	MMP-3 (−)	MMP-3 (+)	*p*
Age (year, median, IQR)	57 (49-65)	63 (53-70)	0.01
Female / Male	73 / 27	69 / 13	0.07
RA duration (year, median, IQR)	5 (3-9)	7 (4-15)	0.17
RF positive (%)	52.6	76.9	< 0.01
ACPA positive (%)	54.4	75.0	0.02
RF & ACPA positive (%)	43.9	69.2	< 0.01
MMP-3 baseline (week 0) (ng/ml, median, IQR)	55.0 (44.2-84.6)	119.0 (78.0-159.6)	< 0.01
DAS28 (ESR) (median, IQR)	2.14 (1.75-2.59)	2.57 (2.12-3.31)	0.02
CDAI (median, IQR)	2.00 (0.70-5.88)	3.50 (1.40-6.60)	0.52
PSL use, n (%)	17 (17.0)	47 (57.3)	< 0.01
mTSS baseline (week 0) (median, IQR)	8.0 (2.0-33.0)	18.5 (7.0-52.0)	0.1
ΔmTSS	0.46 ± 1.12	0.97 ± 1.99	0.03
0.5 ≦ Δ baseline, n	23	35	
progression ratio	23.0	42.7	< 0.01
Without PSL use at baseline, n	77	36	
Δ mTSS	0.51 ± 1.22	1.03 ± 1.90	0.09
0.5 ≦ Δ baseline, n	19	17	
progression ratio	24.7	47.2	0.03
no swollen joints group, n	58	39	
ΔmTSS	0.37 ± 0.89	1.18 ± 2.45	0.02
0.5 ≦ Δ baseline, n	12	17	
progression ratio	20.7	43.6	0.02
PSL use, n (%)	9 (15.5)	19 (48.7)	< 0.01

Data are mean ± S.D. or median (IQR)
RA, rheumatoid arthritis; RF, rheumatoid factor; ACPA, anti-cyclic citrullinated peptide antibodies; MMP-3, matrix metalloproteinase-3; DAS28, Disease Activity Score 28-joint assessment; CDAI, Clinical Disease Activity Index; mTSS, modified Total Sharp Score; PSL, prednisolone.

who were PSL-free. Among these patients, progression of joint destruction was observed in 27.1% and 54.5% (p = 0.03), the ΔmTSS values were 0.49 ± 1.15 and 1.39 ± 2.23 (p = 0.03), and the nonprogression rates were 72.9% and 45.5%, respectively. Similarly, 128 of 182 patients with RA (MMP-3(−), n = 70; MMP-3(+), n = 58) who had achieved LDA or clinical remission (CDAI ≦ 2.8) were compared. The progression of joint destruction was found in 24.3% (MMP-3(−)) and 48.3% (MMP-3(+)) (p < 0.01), the ΔmTSS values were 0.36 ± 0.83 and 1.19 ± 2.23 (p < 0.01), and the nonprogression rates (ΔmTSS < 0.5) were 75.7% and 51.7%, respectively. We further examined the progression of joint destruction in 81 of these 128 patients (MMP-3(−), n = 52; MMP-3(+), n = 29) who were PSL-free. Among these patients, we observed progression of joint destruction in 26.9% and 48.3% (p = 0.08); the ΔmTSS values were 0.42 ± 0.93 and 1.19 ± 2.03 (p = 0.02); and the nonprogression rates were 73.1% and 51.7%, respectively. Joint destruction was more severe in the MMP-3(+) group than in the MMP-3(−) group (**Table 4**), indicating that neither the achievement of LDA nor clinical remission is sufficient to prevent the progression of joint destruction, particularly when the serum MMP-3 levels remain positive.

6. Effect of PSL-induced elevation in MMP-3 on progression of joint destruction

Within the MMP-3(+) group, progression of joint de-

Table 4 In LDA and clinical remission group, MMP-3 (−) or (+) patients analysis at 1-year

	MMP-3 (−)	MMP-3 (+)	*p*
DAS-28 :			
LDA and clinical remission group, n	63	46	
DAS28 (ESR) (median, IQR)	2.09 (1.71-2.44)	2.31 (1.88-2.79)	0.04
mTSS baseline (week 0) (median, IQR)	9.5 (3.1-33.0)	14.5 (5.3-44.0)	0.37
ΔmTSS	0.42 ± 1.02	1.21 ± 2.41	0.02
0.5 ≦ Δ baseline, n	16	23	
PSL use at baseline, n (%)	15 (23.8)	24 (52.2)	
progression ratio	25.4	50.0	< 0.01
DAS-28 (without PSL use at baseline) :			
LDA and clinical remission group, n	48	22	
DAS28 (ESR) (median, IQR)	2.04 (1.70-2.43)	2.31 (1.81-2.79)	0.17
mTSS baseline (week 0) (median, IQR)	8.0 (2.5-31.0)	8.75 (5.3-17.0)	0.42
ΔmTSS	0.49 ± 1.15	1.39 ± 2.23	0.03
0.5 ≦ Δ baseline, n	13	12	
progression ratio	27.1	54.5	0.03
CDAI :			
LDA and clinical remission group, n	70	58	
CDAI (median, IQR)	1.90 (0.63-3.50)	3.10 (1.33-4.80)	0.08
mTSS baseline (week 0) (median, IQR)	10.0 (3.0-38.0)	16.0 (5.3-44.0)	0.72
ΔmTSS	0.36 ± 0.83	1.19 ± 2.23	< 0.01
0.5 ≦ Δ baseline, n	17	28	
PSL use at baseline, n (%)	18 (25.7)	29 (50.0)	
progression ratio	24.3	48.3	< 0.01
CDAI (without PSL use at baseline) :			
LDA and clinical remission group, n	52	29	
CDAI (median, IQR)	1.90 (0.68-3.80)	2.80 (1.20-4.50)	0.36
mTSS baseline (week 0) (median, IQR)	8.5 (3.3-42.8)	8.0 (5.0-19.1)	0.19
ΔmTSS	0.42 ± 0.93	1.19 ± 2.03	0.02
0.5 ≦ Δ baseline, n	14	14	
progression ratio	26.9	48.3	0.08

Data are mean ± S.D. or median (IQR)
DAS28, Disease Activity Score 28-joint assessment; ESR, erythrocyte sedimentation rate; mTSS, modified Total Sharp Score; LDA, low Disease Activity; CDAI, Clinical Disease Activity Index; PSL, prednisolone.

struction was assessed in patients treated with (n = 47) and without (n = 35) PSL. Progression of joint destruction was observed in 51.4% (n = 18) and 40.4% (n = 19) (p = 0.37) in the PSL(−) and PSL(+) groups, ΔmTSS values were 1.13 ± 1.93 and 0.85 ± 2.05 (p = 0.54) (**Figure 2A**), and the incidences of nonprogression were 48.6% and 59.6% (**Figure 2B**).

We then examined whether PSL-induced increases in MMP-3 were associated with progression of joint destruction in MMP-3-positive RA patients who achieved low disease activity or clinical remission (DAS28-ESR < 3.2 or CDAI ≤ 10.0). In patients who achieved LDA or clinical remission based on a DAS28-ESR, progression of joint destruction was observed in 52.2% (n = 11) and 47.8% (n = 12) (p = 1.00) in the PSL(−) and PSL(+) groups, and the incidences of nonprogression were 47.8% and 52.2%. Similarly, of patients who achieved LDA or clinical remission based on a CDAI, progression of joint destruction was observed in 50.0% (n = 15) and 44.4% (n = 12) (p = 0.79) in the PSL(−) and PSL(+) groups, and the incidences of nonprogression were 50.0% and 55.6%. These results indicate that achieving LDA or clinical remission is not sufficient to prevent the progression of joint destruction when MMP-3 remain positive. This suggests the increases in MMP-3 contributed similarly to the progression of joint destruction whether or nor they were related to PSL administration.

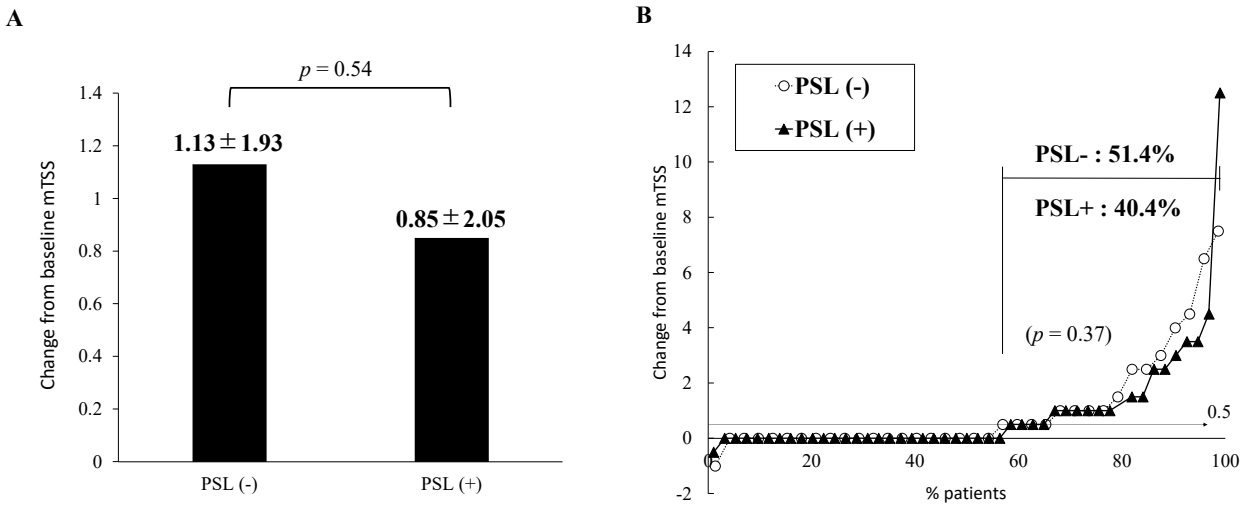

Figure 2 Progression of joint destruction in MMP-3+ patients after 1 year of treatment with or without PSL
(A) ΔmTSS. Values are the mean (SD) at each time point and in the PSL(−) or PSL(+) group. (B) mTSS cumulative probability plot. Percentages indicate the incidences of joint destruction progression (ΔmTSS > 0.5) in each treatment group. (n = 82)

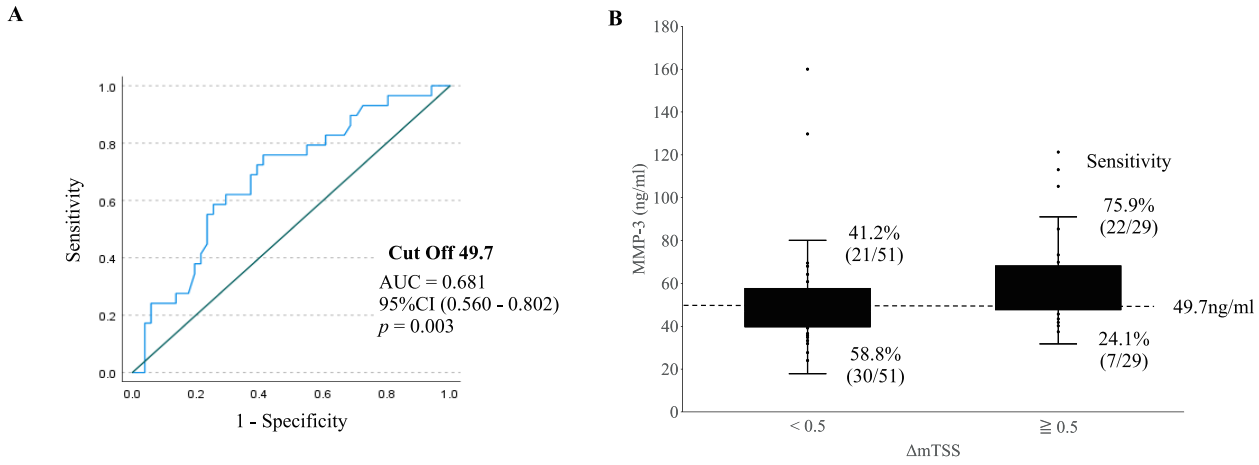

Figure 3 ROC analysis to determine the cut-off value of serum MMP-3 levels
(A) The ROC analysis revealed the cut-off value of the serum MMP-3 was 49.7 ng/mL (area under the curve: 0.681, 95%CI: 0.560–0.802, p < 0.01) to achieve ΔmTSS < 0.5. (B) In the group of patients with advanced joint destruction (ΔmTSS ≥ 0.5), patients had serum MMP-3 levels more than 49.7 ng/mL.

7. ROC analysis to determine the cut-off value of MMP-3 levels

Because of the suggested association between MMP-3 and the rate of joint destruction progression as above, we examined the optimal MMP-3 cut-off value using the ROC curve with the Youden index to determine a practical value for clinical criteria. PSL-free female patients were selected because serum MMP-3 levels are affected by sex (the upper limits of the currently used reference range for male and female are 121.0 and 59.7 ng/mL, respectively) and treatment with or without PSL.

As a result, The ROC analysis revealed that the adequate cut-off value of serum MMP-3 level was 49.7 ng/mL (area under the curve, 0.681; 95% CI 0.560–0.802, $p < 0.01$) (**Figure 3A**) to achieve structural remission (ΔmTSS < 0.5). In patients with advanced joint destruction (ΔmTSS ≥ 0.5), few patients had serum MMP-3 levels <49.7 ng/mL (**Figure 3B**). Therefore, in female patients with RA, lowering the serum MMP-3 level to <49.7 ng/mL is desirable to prevent the progression of joint destruction.

IV. DISCUSSION

Progressive joint destruction is often observed during RA treatment, despite normalized serum CRP levels [7]. The authors of an earlier study proposed that residual MMP-3 activity is one of the responsible factors [19]. Our findings indicate there is greater progression of joint destruction in MMP-3(+) than MMP-3(−) patients, despite their RA being well controlled by MTX therapy, as evidenced by normalized CRP levels and the absence of swollen joints after 1-year of treatment. Moreover, in this study, there were no significant differences in disease activity between the joint destruction(+) and the joint destruction(−) groups. These results suggest that persistently elevated MMP-3 levels lead to joint destruction in patients with RA, including those in remission or with LDA.

During RA treatment, PSL administration is considered to provide a good therapeutic effect when used at appropriate doses [6)20)]. However, MMP-3 levels tend to increase via an unknown mechanism in patients receiving PSL [16)17)]. In our study, there was a positive correlation between PSL dose and MMP-3 value ($r = 0.53$). If this observed PSL-induced elevation in MMP-3 is not related to the pathophysiology of RA, the MMP-3 levels truly derived from the disease pathophysiology should be lower in PSL(+) than in PSL(−) patients, and greater progression of joint destruction should be seen in PSL(−) than PSL(+) patients when their MMP-3 levels are similar. However, our results show that there was no significant difference in mean ΔmTSS and/nor incidences of joint destruction progression between PSL(+) and PSL(−) patients with similar MMP-3 levels. To exclude the possibility that PSL was administered more frequently to patients with high disease activity, we evaluated the progression of joint destruction in MMP-3-positive RA patients who achieved low disease activity or clinical remission (DAS28-ESR < 3.2 or CDAI ≤ 10.0) and found no significant difference in mean ΔmTSS and/nor incidences of joint destruction progression between PSL(−) and PSL(+) patients. Taken together, these findings suggest that PSL-induced increases in MMP-3 levels are also involved in the progression of joint destruction. To our best knowledge, this is the first report to show that PSL induced increases in MMP-3 levels contribute to joint destruction and that PSL is a possible confounding factor in the treatment of RA.

Interestingly, when we selected patients in remission or with LDA at baseline, the MMP-3(+) group had significantly higher mean ΔmTSS and incidences of joint destruction progression than the MMP-3(−) group. Although joint destruction reportedly correlates with disease activity [21)], our results suggest that MMP-3 levels are a more important indicator of radiographic progression of joint destruction. There was no correlation between DAS28 and MMP-3 or between CDAI and MMP-3 in patients in remission or exhibiting LDA (data not shown). Those results also suggest that MMP-3 levels serve as an indicator of joint destruction and imply that even with reduced inflammation and achievement of LDA or remission, joint destruction may continue to progress unless MMP-3 levels are appropriately managed.

Previous studies have reported cut-off values for serum MMP-3 levels to prevent joint destruction [22)23)]. These studies included RA patients with positive CRP values, high disease activity, and receiving PSL treatment. Furthermore, these studies calculated the cut-off value from a patient cohort comprising both sexes, despite different upper limit values of the reference range. In the present study, we analyzed the cut-off values for PSL-free female patients with negative CRP values and in remission or LDA. In the ROC analysis, the appropriate cut-off value of serum MMP-3 levels was found to be 49.7 ng/mL for preventing the progression of joint destruction in these patients; this value falls below the upper reference limit (59.7 ng/mL). Serum MMP-3 levels may be a better indicator of whether joint destruction is likely to progress and suggest treatment intensification, even if disease activity and CRP levels have remained low for up to 1

year. The current reference range of serum MMP-3 was determined based on reference individuals who met the following conditions: negative CRP values, negative RF values, normal fasting blood sugar levels, and normal liver enzyme test results. However, these conditions do not exclude potential RA patients. Thus, it is not surprising that our cut-off value was lower than the upper reference limit of serum MMP-3 [24].

MMP-3 can activate several other MMPs, including MMP-1, MMP-7, and MMP-9, thereby increasing connective tissue matrix proteolysis [25]. It is thought that these proteases contribute to joint destruction, either directly or indirectly, by degrading the cartilage extracellular matrix [9,11]. Thus, it is difficult to achieve structural remission unless MMP-3 levels are reduced to an appropriate level. However, there are currently no therapeutic agents that directly lower MMP-3 levels. In our in vitro experiment, TNF-alpha-induced increase in MMP-3 levels from RA synoviocytes was inhibited by PSL (data not shown); however, oral PSL administration increases MMP-3 levels in vivo [17]. It is necessary to elucidate the mechanism of the PSL-induced increase in MMP-3 levels to develop new therapeutic agents that lower MMP-3 levels in future.

Limitations

This study has some limitations. The retrospective design limits the ability to draw causal inferences. The sample size is relatively small, and the sample is from two university hospitals in the Kansai area of Japan, which may limit generalizability. Joint destruction occurring over a period longer than 1 year was not estimated.

Conclusion

Our study indicates that residual MMP-3 activity may lead to progression of joint destruction in RA patients, even when they achieve clinical remission or LDA through successful treatment with MTX, and that PSL-induced serum MMP-3 increase contribute similarly to the joint destruction compared with the MMP-3 increase without PSL administration. It is also suggested that the clinically relevant cut-off value to achieve the structural remission in female RA patients is 49.7 mg/ml, well under the upper limit of reference range. The development of therapeutic strategies to regulate MMP-3 expression may be necessary to achieve both clinical and structural remission in RA management.

Funding

Open access funding provided by the Hyogo Medical University.

Statements and Declarations:

Competing Interests

The Department of Advanced Medicine for Rheumatic Diseases in Kyoto University is supported by Nagahama City, Shiga, Japan, Toyooka City, Hyogo, Japan, and four pharmaceutical companies (Chugai Pharmaceutical Co. Ltd, UCB Japan Co. Ltd, AYUMI Pharmaceutical Co., and Asahi Kasei Pharma Corp.). The abovementioned pharmaceutical companies were not involved in the study design, data collection and analysis, manuscript writing, or manuscript submission.

KMurakami received speaker fees and/or consulting fees from Eisai Co. Ltd., Chugai Pharmaceutical Co. Ltd., Pfizer Inc., Bristol-Myers Squibb, UCB Japan Co. Ltd., and Astellas Pharma Inc.

AO received research grants and/or speaker fees from Pfizer Inc., Bristol-Myers Squibb., Advantest, Asahi Kasei Pharma Corp., Chugai Pharmaceutical Co. Ltd., Eli Lilly Japan K. K., Ono Pharmaceutical Co., UCB Japan Co., Eisai Co. Ltd., AbbVie Inc., Takeda Pharmaceutical Co. Ltd.

TF received speaker fees from AbbVie, Asahi Kasei, Jansen, and Eisai.

KMurata received speaker and/or consulting fees from AbbVie G.K., Eisai Co., Ltd., Pfizer Inc., Chugai Pharmaceutical Co., Ltd., Pfizer Inc., Bristol-Myers Squibb, and Asahi Kasei Pharma Corp.

MT received research grants and speaker fees from AbbVie G.K., Asahi Kasei Pharma Corporation, Astellas Pharma Inc., Chugai Pharmaceutical Co., Ltd., Eisai Co., Ltd., Eli Lilly and Company, Pfizer Inc., UCB Japan Co., Ltd., Janssen Pharmaceutical K.K., Kyowa Kirin Co., Ltd., Taisho Pharma Co., Ltd., and Teijin Pharma, Ltd.

AM received honorarium from AbbVie G.K., Chugai Pharmaceutical Co. Ltd., Eli Lilly Japan K.K., Eisai Co. Ltd., Pfizer Inc., Bristol-Myers Squibb., Astellas Pharma Inc., and Gilead Sciences Japan.

AM received research grants from AbbVie G.K., Asahi Kasei Pharma Corp., Chugai Pharmaceutical Co. Ltd., and Eisai Co. Ltd. for work outside the scope of this study.

HK, MM, MN, and MK declare no potential conflicts of interest.

Contributions

H.K., M.M., and M.K. contributed to design, data acquisition and analysis, statistical calculations and manuscript writing. K. Murakami, A.O., T.F., K. Murata, M.T., A.M., and M.N. contributed to data analysis. All

authors have read and approved the final manuscript.

Acknowledgements

The authors thank the patients and medical staff of both hospitals for their contribution to this study. We would like to extend our heartfelt gratitude to Michie Asada, Haruo Horii, Naohiro Ito, and Masatoshi Fujii for their generous (financial) support for the KURAMA cohort. The funders were not involved in the study design, data collection, analysis, interpretation of the data, writing of the manuscript, or in any decision to publish the results. We also thank MSTEditing Company (https://www.mstediting.com) for the English language review.

References

1) Koch AE. The pathogenesis of rheumatoid arthritis. Am J Orthop (Belle Mead NJ). 2007; 36: 5-8.
2) Smolen JS, Aletaha D, Bijlsma JWJ, et al. Treating rheumatoid arthritis to target: Recommendations of an international task force. Ann Rheum Dis. 2010; 69 (4): 631-7.
3) Smolen JS, Breedveld FC, Burmester GR, et al. Treating rheumatoid arthritis to target: 2014 update of the recommendations of an international task force. Ann Rheum Dis. 2016; 75 (1): 3-15.
4) Cronstein BN. Low-dose methotrexate : a mainstay in the treatment of rheumatoid arthritis. Pharmacol Rev. 2005; 57 (2): 163-72.
5) Pincus T, Yazici Y, Sokka T, et al. Methotrexate as the "anchor drug" for the treatment of early rheumatoid arthritis. Clin Exp Rheumatol. 2003; 21 (5 Suppl 31): S179-85.
6) Smolen JS, Landewé RBM, Bijlsma JWJ, et al. EULAR recommendations for the management of rheumatoid arthritis with synthetic and biological disease-modifying antirheumatic drugs: 2019 update. Ann Rheum Dis. 2020; 79 (6): 685-99.
7) Smolen JS, Van Der Heijde DM, St Clair EW, et al. Predictors of joint damage in patients with early rheumatoid arthritis treated with high-dose methotrexate with or without concomitant infliximab: Results from the ASPIRE trial. Arthritis Rheum. 2006; 54 (3): 702-10.
8) Malemud CJ. Matrix metalloproteinases (MMPs) in health and disease: an overview. Fron Biosci. 2006; 11: 1696-701.
9) Yoshihara Y, Nakamura H, Obata K, et al. Matrix metalloproteinases and tissue inhibitors of metalloproteinases in synovial fluids from patients with rheumatoid arthritis or osteoarthritis. Ann Rheum Dis. 2000; 59 (6): 455-61.
10) Cawston T. Matrix metalloproteinases and TIMPs: Properties and implications for the rheumatic diseases. Mol Med Today 1998; 4 (3): 130-7.
11) Okada Y. Matrix-degrading metalloproteinases and their roles in joint destruction. Mod Rheumatol. 2000; 10 (3): 121-8.
12) Lerner A, Neidhöfer S, Reuter S, et al. MMP3 is a reliable marker for disease activity, radiological monitoring, disease outcome predictability, and therapeutic response in rheumatoid arthritis. Best Pract Res Clin Rheumatol. 2018; 32 (4): 550-62.
13) Kobayashi A, Naito S, Enomoto H, et al. Serum levels of matrix metalloproteinase 3 (stromelysin 1) for monitoring synovitis in rheumatoid arthritis. Arch Pathol Lab Med. 2007; 131 (4): 563-70.
14) Hattori Y, Kida D, Kaneko A. Normal serum matrix metalloproteinase-3 levels can be used to predict clinical remission and normal physical function in patients with rheumatoid arthritis. Clin Rheumatol. 2019; 38 (1): 181-7.
15) Yoshimi R, Hama M, Takase K, et al. Ultrasonography is a potent tool for the prediction of progressive joint destruction during clinical remission of rheumatoid arthritis. Mod Rheumatol. 2013; 23 (3): 456-65.
16) Hattori Y, Kida D, Kaneko A. Steroid therapy and renal dysfunction are independently associated with serum levels of matrix metalloproteinase-3 in patients with rheumatoid arthritis. Mod Rheumatol 2018; 28 (2): 242-8.
17) Ribbens C, Martin y Porras M, Franchimont N, et al. Increased matrix metalloproteinase-3 serum levels in rheumatic diseases: Relationship with synovitis and steroid treatment. Ann Rheum Dis. 2002; 61 (2): 161-6.
18) Bruynesteyn K, Boers M, Kostense P, et al. Deciding on progression of joint damage in paired films of individual patients: Smallest detectable difference or change. Ann Rheum Dis. 2005; 64 (2): 179-82.
19) Konishi H, Kanou SE, Yukimatsu R, et al. Adenosine inhibits TNFα-induced MMP-3 production in MH7A rheumatoid arthritis synoviocytes via A_{2A} receptor signaling. Sci Rep. 2022; 12 (1): 6033.
20) Kirwan JR. The effect of glucocorticoids on joint destruction in rheumatoid arthritis. The Arthritis and Rheumatism Council Low-Dose Glucocorticoid Study Group. N Engl J Med. 1995; 333 (3): 142-6.
21) Tsuji H, Yano K, Furu M, et al. Time-averaged disease activity fits better joint destruction in rheumatoid arthritis. Sci Rep. 2017; 7 (1): 5856.
22) Mamehara A, Sugimoto T, Sugiyama D, et al. Serum matrix metalloproteinase-3 as predictor of joint destruction in rheumatoid arthritis, treated with non-biological disease modifying anti-rheumatic drugs. Kobe J Med Sci. 2010; 56 (3): E98-107.
23) Maksymowych WP, Landewé R, Conner-Spady B, et al. Serum matrix metalloproteinase 3 is an independent predictor of structural damage progression in patients with ankylosing spondylitis. Arthritis and Rheumatism 2007; 56 (6): 1846-53.
24) Nakata Y, Tanaka Y, Nogami S, et al. Basic study of reagents

for measurement of matrix metalloproteinase-3. Japanese Journal of Medical Technology. 2014; 63(5): 579-85. (in Japanese)

25) Ogata Y, Enghild JJ, Nagase H. Matrix metalloproteinase 3 (stromelysin) activates the precursor for the human matrix metalloproteinase 9. J Biol Chem. 1992; 267(6): 3581-4.